

Astrobiology Manuscript Central: <http://mc.manuscriptcentral.com/astrobiology>

Spatial heterogeneity of thrombolites using molecular, biochemical, and stable isotope analyses

Journal:	<i>Astrobiology</i>
Manuscript ID	Draft
Manuscript Type:	Research Articles (Papers)
Date Submitted by the Author:	n/a
Complete List of Authors:	Louyakis, Artemis; University of Florida, Microbiology and Cell Science Mobberley, Jennifer; University of Florida, Microbiology and Cell Science Vitek, Brooke; University of Miami, Rosenstiel of Marine and Atmospheric Sciences Visscher, Pieter; UCONN, Marine Sciences Hagan, Paul; University of Miami, Rosenstiel of Marine and Atmospheric Sciences Reid, Pamela; University of Miami, Rosenstiel of Marine and Atmospheric Sciences Kozdon, Reinhard; Columbia University, Lamont-Doherty Earth Observatory; Univeristy of Wisconsin, Department of Geoscience Orland, Ian; Univeristy of Wisconsin, Department of Geoscience Valley, John; Univeristy of Wisconsin, Department of Geoscience Planavsky, Noah; Yale University, Department of Geology and Geophysics Casaburi, Giorgio; University of Florida, Microbiology and Cell Science Foster, Jamie; University of Florida, Microbiology and Cell Science
Keyword:	Microbe-Mineral Interactions, Microbial Mats, Cyanobacteria, Stable Isotopes
Note: The following files were submitted by the author for peer review, but cannot be converted to PDF. You must view these files (e.g. movies) online.	
Table S2_PICRUSSt_071316.csv TableS4_18O_071216page1.csv TableS4_18O_071216page2.csv TableS5_13C_071316page1.csv TableS5_13C_071316page2.csv	

1
2
3 1 Spatial heterogeneity of thrombolites using molecular, biochemical, and stable isotope
4
5 2 analyses
6
7 3

8
9
10 4 Artemis S. Louyakis¹, Jennifer M. Mobberley¹, Brooke E. Vitek², Pieter T. Visscher³, Paul D.
11 5 Hagan², R. Pamela Reid², Reinhard Kozdon^{4,5}, Ian J. Orland⁵, John W. Valley⁵, Noah J.
12 6 Planavsky⁶, Giorgio Casaburi¹, and Jamie S. Foster^{1*}
13
14
15
16
17
18
19
20
21
22

23 10 Running Title: Spatial organization of unlaminated thrombolites
24
25
26
27
28
29
30
31
32
33

34 12 ¹Department of Microbiology and Cell Science, University of Florida, Space Life Sciences
35 13 Lab, Merritt Island, Florida
36
37
38
39
40
41
42
43
44
45
46

47 14 ²Rosenstiel School of Marine and Atmospheric Science, University of Miami, Miami, Florida

48 15 ³Department of Marine Sciences, University of Connecticut, Groton, Connecticut

49 16 ⁴Lamont-Doherty Earth Observatory, Columbia University, Palisades, New York

50 17 ⁵Department of Geoscience, University of Wisconsin, Madison, Wisconsin

51 18 ⁶Department of Geology and Geophysics, Yale University, New Haven, Connecticut
52
53
54
55
56
57
58
59
60

21 *Corresponding Author:

22 Tel: 321-525-1047; Email: jfoster@ufl.edu

1
2
3 **23 Abstract**
4

5 24 Thrombolites are build-ups of carbonate, exhibiting a clotted internal structure, formed
6
7 25 through the interactions of microbial mats and their environment. Despite recent advances,
8
9 26 we are only beginning to understand the microbial and molecular processes associated with
10
11 27 their formation. In this study, a spatial profile of the microbial and metabolic diversity of
12
13 28 thrombolite-forming mats of Highborne Cay, The Bahamas was generated using 16S rRNA
14
15 29 gene sequencing and predictive metagenomic analyses. These molecular-based approaches
16
17 30 were complemented with microelectrode profiling and *in situ* stable isotope analysis to
18
19 31 examine the dominant taxa and metabolic activities within the thrombolite-forming
20
21 32 communities. Results revealed three distinctive zones within the thrombolite-forming mats
22
23 33 that exhibited stratified populations of bacteria and archaea. Predictive metagenomics also
24
25 34 revealed vertical profiles of metabolic capabilities, such as photosynthesis, carboxylic and
26
27 35 fatty acid synthesis within the mats. The carbonate precipitates within the thrombolite-
28
29 36 forming mats exhibited isotopic geochemical signatures suggesting that the precipitation
30
31 37 within the Bahamian thrombolites is photosynthetically induced. Together, this study serves
32
33 38 as a foundation to begin to correlate the distribution of microbes and their activities within
34
35 39 modern thrombolite systems to further understand their formation.
36
37
38
39
40
41
42

43 41 Key words: thrombolites, microbial diversity, metagenome, stable isotopes, microbialites
44
45 42
46
47 43
48
49
50
51
52
53
54
55
56
57
58
59
60

1. Introduction

With their long evolutionary history, microbialites serve as important model systems to explore and understand the co-evolutionary dynamics between lithifying microbial communities and their local environment. These carbonate structures are formed via the metabolic activity of microbes, which influence and drive biological processes associated with sediment capture and biologically induced mineralization. Microbialites have been found in a wide range of habitats including brackish (e.g., Laval *et al.*, 2000; Breitbart *et al.*, 2009; White *et al.*, 2015), marine (e.g., Dravis, 1983; Reid *et al.*, 2000; Stolz *et al.*, 2009; Casaburi *et al.*, 2016), and hypersaline (e.g., Logan 1961; Glunk *et al.*, 2011; Wong *et al.*, 2015; Suosaari *et al.*, 2016; Paul *et al.*, 2016) environments and are classified based on their internal microfabrics (Burne and Moore, 1987; Dupraz *et al.*, 2009). Two of the most well-studied types of microbialites are stromatolites, which exhibit laminated internal fabrics (Reid *et al.*, 2000), and thrombolites with irregular clotted fabrics (Aitken, 1967; Kennard and James, 1986).

Much of our understanding of microbialite formation comes from study of modern systems (e.g., Reid *et al.*, 2000; Saghaï *et al.*, 2015; Casaburi *et al.*, 2016; White *et al.*, 2015; Warden *et al.*, 2016; White *et al.*, 2016). Microbialites in The Bahamas have been particularly important in expanding research in this area, as they are the only known modern open marine microbialite system. In Bahamian stromatolites, processes underlying formation include iterative growth by cycling microbial mat communities and seasonal environmental controls; the resulting lamination represents a chronology of past surface communities (Visscher *et al.*, 1998; Reid *et al.*, 2000; Bowlin *et al.*, 2012). In thrombolites, the processes that form the clotted fabrics are not well defined. In some Bahamian thrombolites, the clots appear to be products of calcified cyanobacterial filaments, which through their metabolism cause shifts in the carbonate saturation state and thereby drive precipitation (Dupraz *et al.*,

69 2009; Planavsky *et al.*, 2009; Myshrall *et al.*, 2010). Alternatively, it has been suggested that
70 the clotted texture in thrombolites is linked to disruption or modification of microbial fabrics
71 (Planavsky and Ginsburg, 2009; Bernhard *et al.*, 2013; Edgcomb *et al.*, 2013).

72 To further explore the formation of clotted fabrics, the marine thrombolites of
73 Highborne Cay, The Bahamas were targeted as they represent one of the few modern
74 locations of actively accreting thrombolitic microbialites (Planavsky *et al.*, 2009; Myshrall *et*
75 *al.*, 2010; Mobberley *et al.*, 2012; Mobberley *et al.*, 2013; Mobberley *et al.*, 2015). These
76 thrombolites form in the intertidal zone of a 2.5 km fringing reef complex that extends along
77 the eastern margin of Highborne Cay (Fig. 1A; Reid *et al.*, 1999). The thrombolites range in
78 size from up to one meter in height to several meters in length (Andres and Reid, 2006;
79 Myshrall *et al.*, 2010) and are covered with several distinct microbial mat types (Mobberley
80 *et al.*, 2012).

81 The dominant mat type associated with these thrombolites, referred to as ‘button’ mat,
82 harbors tufts of vertically orientated calcified cyanobacterial filaments (Fig. 1B; Myshrall *et*
83 *al.*, 2010; Mobberley *et al.*, 2012). The dominant cyanobacterium identified within these
84 tufts, using both morphological and molecular tools, is *Dichothrix* sp. (Planavsky *et al.*, 2009;
85 Mobberley *et al.*, 2012). At the surface, these *Dichothrix*-enriched button mats are calcified
86 with aragonite precipitates located within the exopolymeric sheath of the cell. With depth,
87 precipitates undergo dissolution and filaments degrade (Planavsky *et al.*, 2009). In addition to
88 the tufts of calcified filaments, the thrombolite-forming button mats also harbor a genetically
89 diverse and active microbial community that appears to form vertical gradients of metabolic
90 activity (Myshrall *et al.*, 2010; Mobberley *et al.*, 2013; Mobberley *et al.*, 2015).

91 Previous work in other microbialite systems, such as stromatolites, has shown that the
92 relationship between active, distinct microbial guilds can alter the local physiochemical
93 environment and generate discrete gradients of both solutes and redox conditions (e.g.,

1
2
3 94 Dupraz *et al.*, 2009; Glunk *et al.*, 2011; Wong *et al.*, 2015). Within these microenvironments
4
5 95 the microbial activity can alter both the carbonate saturation index (i.e., carbonate alkalinity
6
7 96 and availability of free calcium) and the cycling of exopolymeric substances (EPS; Braissant
8
9 97 *et al.*, 2009), which serve as important nucleation sites for precipitation (Dupraz and
10
11 98 Visscher, 2005). Certain metabolisms, such as photosynthesis and some types of sulfate
12
13 99 reduction, can lead to an increase in pH and thereby promote precipitation (Visscher *et al.*,
14
15 100 1998; Dupraz *et al.*, 2009; Gallagher *et al.*, 2012). Contrastingly, some metabolisms, such as
16
17 101 sulfide oxidation, aerobic respiration and fermentation, can increase dissolved inorganic
18
19 102 carbon (DIC) concentrations but lower the pH and carbonate saturation state of the local
20
21 103 environment and promote dissolution (Walter *et al.*, 1994; Visscher *et al.*, 1998; Dupraz *et*
22
23 104 *al.*, 2009). Together it is the parity between metabolisms that determines the extent and net
24
25 105 precipitation potential within the lithifying mat community (Visscher and Stolz, 2005).
26
27
28

29
30 106 In addition to the precipitation potential, another component that is critical to the
31
32 107 formation of microbialites is the availability of nucleation sites, which can be controlled by
33
34 108 the production and degradation of EPS material. The EPS matrix serves several essential
35
36 109 roles in the formation of microbialites as it binds cations (e.g., Ca^{2+}) critical for carbonate
37
38 110 precipitation, serves as attachment sites for microbes to withstand the high energy wave
39
40 111 impacts, and protects microbes from environmental stresses, such as UV exposure and
41
42 112 desiccation (Dupraz *et al.*, 2009). Metagenomic analyses of both stromatolites and
43
44 113 thrombolites across the globe have shown that Cyanobacteria and Proteobacteria are the two
45
46 114 primary producers of EPS material (Khodadad and Foster, 2012; Mobberley *et al.*, 2013;
47
48 115 Mobberley *et al.*, 2015; Casaburi *et al.*, 2016; Ruvindy *et al.*, 2016; Warden *et al.*, 2016).
49
50 116 Alteration or restructuring of the EPS through microbial degradation can reduce the cation-
51
52 117 binding capability and thereby facilitate the precipitation of calcium carbonate on the EPS
53
54 118 matrix (Dupraz *et al.*, 2004; Dupraz and Visscher 2005; Dupraz *et al.*, 2009).
55
56
57
58
59
60

1
2
3 119 There have been major advances in understanding the processes controlling
4
5 120 stromatolite formation; in contrast, the factors controlling carbonate precipitation in
6
7 121 thrombolites are less understood. In this study we build on previous work by examining the
8
9 122 spatial distribution of the bacterial and archaeal diversity associated with the button mats
10
11 123 using a targeted phylogenetic marker gene approach coupled with a predictive computational
12
13 124 reconstruction of the metagenome to ascertain how thrombolite-forming communities
14
15 125 change, both taxonomically and functionally, with depth. These molecular based approaches
16
17 126 are complemented with stable isotope work to provide additional constraints on carbonate
18
19 127 precipitation in the *Dichothis* calcified filaments. Together, these methodologies elucidate
20
21 128 the spatial organization of the taxa associated with the thrombolite-forming mats as well as
22
23 129 delineate their potential metabolic function in these lithifying ecosystems.
24
25
26
27
28
29

30 131 **2. Methods**

31 132 *2.1. Sample collection*

32
33
34 133 Thrombolite-forming button mats were collected from the island of Highborne Cay, The
35
36 134 Bahamas (76°49' W, 24°43'N) in February 2010 and October 2013 from an intertidal
37
38 135 thrombolitic platform from Site 5 (Andres and Reid, 2006). The 2010 mats were partitioned
39
40 136 in the field into three distinct vertical sections (0 – 3 mm; 3 – 5 mm; and 5 – 9 mm depth
41
42 137 horizons, respectively) and immediately placed into RNAlater (Life Technologies, Inc.,
43
44 138 Grand Island, NY). These samples were transported to Space Life Sciences Lab, Merritt
45
46 139 Island, FL where they were stored at -80°C until processing. The 2013 mats were processed
47
48 140 for isotope analyses as described below.
49
50
51
52
53
54
55
56
57
58
59
60

1
2
3 144 *2.2. Microelectrode measurements*

4
5 145 Depth profiles of oxygen, sulfide and pH were determined in triplicate using needle
6
7 146 microelectrodes (Visscher *et al.*, 1991, 1998; Pages *et al.*, 2014) either *in situ* or *ex situ* under
8
9
10 147 ambient temperature and light intensity. Microelectrodes with a tip diameter between 60 and
11
12 148 150 μm were deployed in 250 μm depth increments using a manual micromanipulator
13
14 149 (National Aperture, Salem, NH). Oxygen profiles were measured in submerged mats (in ca.
15
16 150 5-15 cm water) using a polarographic Clark-type needle electrode with an outer diameter of
17
18 151 0.4 mm and readings were recorded with a picoammeter (PA2000; Unisense, Aarhus,
19
20 152 Denmark). Polarographic sulfide electrodes (Unisense, Denmark) were used in combination
21
22 153 with a Unisense PA 2000 picoammeter, and pH and S^{2-} electrodes (Diamond General, Ann
23
24 154 Arbor, MI) were connected to a high-impedance millivolt meter (Microscale Measurements,
25
26 155 The Netherlands). Both electrode types were encased in needles (outer diameter 0.5 mm).
27
28 156 Sulfide electrodes were calibrated before and after each deployment using buffers of three
29
30 157 different pH values that span the pH range observed in the thrombolite (i.e., pH 7, 8 and 9).
31
32 158 Under an oxygen-free atmosphere, aliquots of a sulfide stock solution were added in
33
34 159 increments to the buffer and electrode signals were recorded. Subsamples of the buffer were
35
36 160 taken to ascertain the actual concentration of sulfide in the calibration cocktail using the
37
38 161 methylene blue method. The pH electrodes were calibrated at pH 5, 7 and 10. The pH
39
40 162 profiles were used to calculate the actual sulfide concentration at each depth.
41
42
43
44
45

46
47 164 *2.3. Generation and sequencing of 16S rRNA gene libraries*

48
49 165 DNA was extracted in triplicate from each vertical section using a modified MoBio
50
51 166 PowerSoil DNA isolation kit that included a xanthogenate pre-treatment, as previously
52
53 167 described (Mobberley *et al.*, 2012). The DNA was then PCR amplified in triplicate using
54
55 168 fusion 454-primers that included a unique eight base pair barcode on the 3' end
56
57
58
59
60

1
2
3 169 (Supplemental Table S1). The PCR reactions for the bacterial 16S rRNA libraries targeted
4
5 170 the V1-2 region and included the following: 1 x Pfu Reaction Buffer (Stratagene, La Jolla,
6
7 171 CA), 280 μ M dNTPs, 2.5 μ g bovine serum albumin (BSA), 600 nM of each primer, 1 ng of
8
9 172 genomic mat DNA, 1.25 U of Pfu DNA Polymerase (Stratagene, La Jolla, CA) and nuclease-
10
11 173 free water (Sigma, St. Louis, MO) in a volume of 25 μ l. The amplification parameters
12
13 174 included a 95°C denaturation for 5 min, followed by 30 cycles of 95°C for 1 min, 64°C for 1
14
15 175 min, 75°C for 1 min and a final extension at 75°C for 7 min.
16
17
18

19 176 The archaeal libraries required a nested PCR approach that included two rounds of
20
21 177 amplification and targeted the V3-5 region. The reactions contained the same concentrations
22
23 178 as the bacterial library with the exception of 400 nM of 23F and 958R primers (DeLong,
24
25 179 1992; Barns *et al.*, 1994) and 10 ng of thrombotic mat DNA in round one, whereas 400 nM
26
27 180 of primers 334F and 915R (Casamayor *et al.*, 2002) with 10 ng of round one amplicon
28
29 181 material as a template. The amplification parameters in round one included a denaturation
30
31 182 step of 95°C for 2 min, followed by 35 cycles of 95°C for 30 sec, 55°C for 1 min, 72°C for 2
32
33 183 min with an extension of 72°C for 10 min. In round two the parameters were similar except
34
35 184 that the annealing temperature was changed to 61°C.
36
37
38

39 185 For each library, the PCR amplicons were purified using the Ultraclean PCR Clean-
40
41 186 Up Kit (MoBio, Carlsbad, CA) and combined into equimolar ratios. Sequencing was
42
43 187 performed per manufacturers protocol using a 454 GS-FLX platform with Titanium
44
45 188 chemistry (Roche, Branford, CT) at the University of Florida's Interdisciplinary Center for
46
47 189 Biotechnology Research. The raw sequence data files were deposited into the NCBI
48
49 190 sequencing read archive under number SRP068710 (bacteria) and SRP068710 (archaea)
50
51 191 under project PRJNA305634.
52
53
54

55 192

56
57 193 *2.4. Bioinformatic analysis of 16S rRNA gene libraries*
58
59
60

1
2
3 194 The recovered bacterial and archaeal 16S rRNA gene sequences were analyzed using
4
5 195 Quantitative Insights Into Microbial Ecology (QIIME; version 1.9.1; Caporaso *et al.*, 2010).
6
7 196 Preprocessing was completed to separate the replicate libraries by depth, remove barcode
8
9
10 197 adaptors, and filter for quality using default parameters including: minimum sequence length
11
12 198 of 200 bp; maximum sequence length of 1000 bp; minimum quality score of 25; maximum
13
14 199 ambiguous bases of 6; and maximum homopolymer length of 6. Operational taxonomic units
15
16 200 (OTUs) were assigned to the filtered reads at 97% identity against the Greengenes database
17
18 201 (v13.8; DeSantis *et al.*, 2006) using the UCLUST method within QIIME. Further filtering
19
20 202 was completed including removal of unassigned reads and filtering for most abundant OTUs
21
22 203 (> 0.005%). The generated OTU table was used for taxonomic comparison, filtering the
23
24 204 OTUs at 0.005% and producing taxonomic trees using Meta Genome Analyzer (MEGAN5;
25
26 205 Huson *et al.*, 2007). OTU tables were filtered at 0.1% and hierarchal taxonomic pie charts
27
28 206 were created using the Krona tool (Ondov *et al.*, 2011). The representative sequences were
29
30 207 aligned using PyNAST (v1.2.2; Caporaso *et al.*, 2010) to the Greengenes Core reference
31
32 208 alignment and a phylogenetic tree was built using FastTree (v2.1.3; Price *et al.*, 2010). The
33
34 209 phylogenetic tree was used for downstream community analyses. Diversity analyses were
35
36 210 performed at a sequence depth of 3587 for archaea and 3691 for bacteria.

37
38
39
40
41 211 Alpha diversity indices were calculated using observed species and Faith's
42
43 212 Phylogenetic Diversity (PD) measure (Faith, 1992), and the averaged results were used to
44
45 213 generate rarefaction curves. Beta diversity comparisons were visualized using Principal
46
47 214 Coordinates Analyses (PCoA) using Emperor (Vázquez-Baeza *et al.*, 2013) generated from
48
49 215 unweighted UniFrac distance matrices (Lozupone and Knight, 2005). Statistical significance
50
51 216 between the mat depths was calculated using adonis, a nonparametric, permutation based
52
53 217 metrics.
54
55

56 218
57
58
59
60

1
2
3 219 *2.5. Reconstruction of functional metagenome using the PICRUSt algorithm*

4
5 220 Functional gene content from each of the three vertical sections was predicted from the
6
7 221 recovered 16S rRNA gene sequences using the algorithm Phylogenetic Investigation of
8
9 222 Communities by Reconstruction of Unobserved States (PICRUSt v.1 .0; Langille *et al.*,
10 223 2013), as previously described (Casaburi *et al.*, 2016). Results were collapsed at KEGG
11
12 224 Orthologs (KO) Level 3 within the pathway hierarchy of KEGG (Kanehisa and Goto, 2000).
13
14 225 For comparison purposes a shotgun metagenomic dataset of whole Bahamian thrombolite-
15
16 226 associated mats previously collected from Highborne Cay (Mobberley *et al.*, 2013) was
17
18 227 downloaded from the MG-RAST database with accession number 4513715.3. Raw reads
19
20 228 were filtered using SICKLE (v. 1.2; Joshi and Fass, 2011) with default parameters. Filtered
21
22 229 reads were re-annotated for functionality at different KEGG levels, using the Metagenome
23
24 230 Composition Vector (MetaCV v. 2.3.0) with default parameters (Liu *et al.*, 2012). Resulting
25
26 231 hits were filtered at a correlation score > 30, collapsed at KO Level 3, and finally compared
27
28 232 to the 16S rRNA gene predicted functional profile.
29
30
31
32
33

34 233
35
36 234 *2.6. Bulk stable isotope analysis*

37
38 235 Samples of thrombolite-forming mats were collected from Site 5 (Andres and Reid, 2006) of
39
40 236 Highborne Cay in October 2013. The mat samples were dried and examined using bulk
41
42 237 isotope analysis for both inorganic and organic signatures. Calcified filaments were dissected
43
44 238 from the button mats, dried and ground to a fine powder in triplicate. Aliquots of the
45
46 239 carbonate (i.e., aragonite; Planavsky *et al.*, 2009) were measured for inorganic $\delta^{13}\text{C}$ and $\delta^{18}\text{O}$
47
48 240 using a Finnigan-MAT 252 isotope ratio mass spectrometer coupled with a Kiel III
49
50 241 carbonate preparation device.
51

52 242 For isotopic analysis of organic matter, calcified filaments were dissected and treated
53
54 243 with an acid solution (6N HCl) at room temperature overnight until all CaCO_3 was removed.
55
56
57
58
59
60

1
2
3 244 Samples were loaded into tin capsules and placed in a 50-position automated Zero
4
5 245 Blank sample carousel on a Carlo Erba NA1500 CNHS elemental analyzer. After flash
6
7 246 combustion in a quartz column containing chromium oxide and silvered cobaltous/cobaltic
8
9
10 247 oxide at 1000°C in an oxygen-rich atmosphere, the sample gas was transported in a He
11
12 248 carrier stream and passed through a hot reduction column (650°C) consisting of
13
14 249 reduced elemental copper to remove oxygen. The effluent stream then passed through a
15
16 250 chemical (magnesium perchlorate) trap to remove water followed by a 3 meter GC column at
17
18 251 45°C to separate N₂ from CO₂. The sample gas next passed into a ConFlo II preparation
19
20 252 system and into the inlet of a Thermo Electron Delta V Advantage isotope ratio mass
21
22 253 spectrometer running in continuous flow mode where the sample gas was measured relative
23
24 254 to laboratory reference N₂ and CO₂ gases. All carbon and oxygen isotopic results are
25
26 255 expressed in standard delta notation relative to Vienna Pee Dee Belemnite (VPDB), whereas
27
28 256 nitrogen isotopic results are expressed in standard delta notation relative to air (AIR). The
29
30 257 standard used for bulk C and O measurements was NBS-19, where as USGS40 and USGS41
31
32 258 were used for N. Measurements were conducted in triplicate at the Light Stable Isotope Mass
33
34 259 Spectrometry Laboratory in the Department of Geological Sciences at the University of
35
36 260 Florida. Instrument precision was better than 0.10‰ for all bulk isotope measurements.
37
38
39
40
41
42

43 262 *2.7. Stable isotope analysis using Secondary Ion Mass Spectrometry (SIMS)*

44
45 263 Additional mat samples, collected in Oct 2013, were prepared as thin-sections at the
46
47 264 WiscSIMS laboratory, UW-Madison. Samples were cast with EpoxiCure resin in 25 mm
48
49 265 epoxy rounds, cut with a Buehler IsoMet™ low speed to expose the most suitable section for
50
51 266 analysis, and turned, together with two grains of UWC-3 WiscSIMS calcite standard ($\delta^{13}\text{C} =$
52
53 267 $-0.91 \pm 0.04\text{‰}$; $\delta^{18}\text{O} = -17.87\text{‰} \pm 0.03\text{‰}$ VPDB (Kozdon *et al.*, 2009), into ~100 μm -thick
54
55 268 thin sections. An aragonite standard (UWArg-7, $\delta^{13}\text{C} = 5.99\text{‰}$; $\delta^{18}\text{O} = -10.84\text{‰}$ VPDB;
56
57
58
59
60

1
2
3 269 Orland, 2012; Linzmeier et al., 2016) was also run at the beginning of each day of analysis to
4
5 270 correct for the differences in instrumental mass fractionation between calcite and aragonite,
6
7 271 which was 1.3‰ for $\delta^{18}\text{O}$ and 1.5‰ for $\delta^{13}\text{C}$. The epoxy rounds were ground to expose
8
9 272 features of interest for analysis. Petrographic microscopy was conducted using an Olympus
10
11 273 BH-2 microscope with plane-polarized and cross-polarized transmitted light at various
12
13 274 magnifications to identify potential sites suitable for SIMS analysis. The samples were then
14
15 275 polished and sputter coated with palladium for scanning electron microscopy (SEM) at the at
16
17 276 University of Miami's Center for Advanced Microscopy (UMCAM) to identify areas of
18
19 277 precipitate for analysis and to screen for potential textural anomalies that might impede *in*
20
21 278 *situ* $\delta^{13}\text{C}$ and $\delta^{18}\text{O}$ measurements. The SEM analysis was conducted on a FEI XL-30 Field
22
23 279 Emission ESEM/SEM instrument with energy dispersive spectrometer (EDS). The SEM
24
25 280 analysis was to insure integrity of the sample and to identify specific target sites. After SEM
26
27 281 analysis the palladium coating was removed with 0.25 μm polish on alapidary wheel, dried,
28
29 282 and recoated with gold.
30
31
32
33

34 283 The thrombolite mat samples were then analyzed for $\delta^{13}\text{C}$ and $\delta^{18}\text{O}$ on a CAMECA
35
36 284 ims-1280 secondary ion microprobe mass spectrometer (SIMS) using a $^{133}\text{Cs}^+$ primary ion
37
38 285 beam at the WiscSIMS Laboratory, Department of Geoscience, University of Wisconsin-
39
40 286 Madison. A primary beam of 600 pA, with mean 0.77 % spot-to-spot precision (2SD), was
41
42 287 used for $\delta^{13}\text{C}$, and 1.7 nA was used for $\delta^{18}\text{O}$ with a 10 μm spot size (precision $\sim 0.3\%$).
43
44 288 Details of WiscSIMS carbonate analysis has been described in detail in previous publications
45
46 289 (Orland *et al.*, 2009; Valley and Kita, 2009; Kozdon *et al.*, 2011; Williford *et al.*, 2016).
47
48

49 290 Analysis of the thrombolitic mat sections (10 – 15 spot analyses per sample) were
50
51 291 bracketed by 8 - 10 repeat measurements on the UWC-3 standard grain using the same
52
53 292 parameters as the samples to help determine instrumental mass fractionation corrections for
54
55 293 each set of measurements. After completion of each analytical session, the samples were
56
57
58
59
60

1
2
3 294 returned to University of Miami for SEM inspection of the pits to evaluate any features that
4
5 295 may have impacted accuracy (e.g., cracks or epoxy). Additionally, for those measurements
6
7 296 that penetrated down to epoxy material (depths of 1-2 μm) and had high secondary ion count
8
9 297 rates (i.e., > 100% for ^{12}C of the measured counts per second on the standard grain), the final
10
11 298 three to six cycles (of 20) were excluded from computations and the values for the spots were
12
13 299 recalculated as in Vetter *et al.* (2014). Visualization of the data was conducted in R (v.3.2.2;
14
15 300 R Core Team, 2015) using the package ggplot2 (Wickham, 2009).
16
17
18
19

301

302 **3. Results**

303 *3.1. Microelectrode profiling of thrombolite button mats*

304 The *in situ* concentrations of oxygen and sulfide were measured with microelectrodes during
305 early afternoon representing peak photosynthesis (i.e., 12:30pm and 2:00pm) and at the end
306 of the night, at the end of a prolonged anoxic period (i.e., 4:00am – 6:00am) (Fig. 1C). The
307 profiles revealed steep vertical gradients that fluctuated throughout the diel cycle. During the
308 day, the oxic zone extended through the first 5 mm of the button mat with the peak of oxygen
309 production (> 600 μM) occurring in the upper 3 mm (Fig. 1C). At night, however, oxygen
310 levels decreased significantly and were detectable only in the upper 2 mm of the mat
311 suggesting rapid consumption at night and limited diffusion of O_2 from the overlying water
312 column. Contrastingly, sulfide levels were low during the day with levels detectable only
313 below 6 mm. At night, sulfide levels built-up and were detectable at 4 mm with a peak
314 concentration occurring at a depth of 8 - 10 mm within the mat.

315 In addition to oxygen and sulfide, pH was also monitored throughout the vertical
316 profile of the button mat revealing a wide shift throughout the diel cycle. At peak
317 photosynthesis the localized pH ranged from 8.4 to 10.4 throughout the depth profile with the
318 highest pH occurring at a depth of 3 mm (Fig. 1C). At night, however, the pH steadily

1
2
3 319 decreased to as low as 7.1 at depths below 5 mm. Based on these oxygen, sulfide and pH
4
5 320 microelectrode profiles three distinct spatial zones emerged. Zone 1 included the upper 3
6
7 321 mm of the button mat and contained a supersaturated oxic zone that was suggestive of high
8
9 322 rates of oxygen production and consumption. Zone 2 represented a transitional area 3 – 5 mm
10
11 323 beneath the surface where oxygen levels decreased and sulfide levels began to build. Finally
12
13 324 Zone 3, which included depths below 5 mm, represented a primarily anoxic region of the
14
15 325 thrombolite-forming mat.
16
17 326

20 327 3.2. Phylogenetic composition of Bacteria in thrombolite communities with depth

21
22 328 Immediately after the microelectrode profiles were generated the thrombolite mats were then
23
24 329 sectioned based on these three observed zones (Zone 1, 0 – 3 mm; Zone 2, 3 – 5mm; and
25
26 330 Zone 3, 5 – 9 mm) and each of these distinctive spatial regions was subsequently examined
27
28 331 for taxonomic diversity (Fig. 1D). Three replicate amplicon libraries were generated for each
29
30 332 zone targeting the 16S rRNA gene for both the Bacteria and Archaea. A summary of the data
31
32 333 associated with the amplicon libraries is provided in Table 1. The overall bacterial diversity
33
34 334 increased with depth (Supplemental Fig. S1A) with 2044 operational taxonomic units
35
36 335 (OTUs) at 97% sequencing similarity in the upper oxic Zone 1 and 2947 and 3525 OTUs
37
38 336 recovered from Zone 2 and 3, respectively. The number of recovered OTUs was much higher
39
40 337 than previous diversity assessments of the Highborne Cay thrombolites (Myshrall *et al.*,
41
42 338 2010; Mobberley *et al.*, 2012) and likely reflects the increased sequencing coverage as
43
44 339 determined by Good's estimates (Table 1).

45
46 340 A total of 16 phyla were recovered from the three spatial zones within the
47
48 341 thrombolite-forming mat with the Proteobacteria, Cyanobacteria, Bacteroidetes, Chloroflexi,
49
50 342 and Acidobacteria being highly represented in each zone (Supplemental Fig. S2). Distinct
51
52 343 taxonomic differences, however, were observed between the three spatial regions of the
53
54
55
56
57
58
59
60

1
2
3 344 thrombolite mat at the family level (Fig. 2, 3; Supplemental Fig. S2). In the upper Zone 1, the
4
5 345 most abundant family represented within the mat is the cyanobacterial family Rivulariaceae
6
7 346 (Fig. 2; Supplemental Fig. S2). This taxon contains the genus, *Dichothrix*, previously
8
9
10 347 identified in the thrombolite mats as forming extensive tufts of calcified filaments (Fig. 1B)
11
12 348 and has rarely been found in laminated stromatolites (Foster and Green, 2011). The
13
14 349 Rivulariaceae dominated the oxic Zone 1 comprising 21% of annotated reads compared to
15
16 350 15% in the transitional Zone 2 and only 5% of the total recovered reads in Zone 3 (Fig. 2;
17
18 351 Supplementary Fig. S2). In addition to Rivulariaceae, other prevalent Cyanobacteria in the
19
20
21 352 oxic Zone 1 included Pseudanabaenaceae (11%), Xenococcaceae (5%), and
22
23 353 Synechococcaceae (4%; Fig. 2; Supplemental Fig. S2).

24
25 354 Although Cyanobacteria was the dominant phylum recovered from Zone 1, there was
26
27 355 also a diverse population of Proteobacteria, specifically, the subclass Alphaproteobacteria.
28
29 356 Within the Alphaproteobacteria there was enrichment of the photoheterotrophic
30
31
32 357 Rhodobacteraceae (19%) and Rhodospirillaceae (7%) families, and to a lesser extent the
33
34 358 Rhizobiales (5%). These taxa were not only abundant in Zone 1 but were highly represented
35
36 359 throughout the thrombolite vertical profile (Fig. 3; Supplemental Fig. S2). Other
37
38
39 360 proteobacterial taxa that were abundant in Zone 1 compared to the other two zones included
40
41 361 the sulfate-reducing Deltaproteobacteria family Deltavibrionaceae (3%) and the
42
43 362 Gammaproteobacteria family Thiotrichaceae (0.8%), which harbors several sulfide oxidizing
44
45 363 taxa (Fig. 3). A detailed krona plot of the upper 3 mm of the thrombolite mat is provided in
46
47 364 Supplemental Fig. S3.

48
49
50 365 Zone 2 represented a transitional phase in the thrombolite-forming mats with several
51
52 366 taxa first appearing in this 3 – 5 mm zone and gradually increasing in relative abundance in
53
54 367 the anoxic Zone 3 (Fig. 3; Supplemental Fig. S2, S4). For example, in the
55
56 368 Deltaproteobacteria the sulfate-reducing families Desulfobacteraceae and
57
58
59
60

1
2
3 369 Syntrophobacteraceae were enriched in Zones 2 and 3 compared to Zone 1. Additionally, the
4
5 370 purple sulfur bacterial Gammaproteobacteria family Ectothiorhodospiraceae (order
6
7 371 Chromatiales) and the sulfide-oxidizing Piscirickettsiaceae (order Thiotrichales) also
8
9
10 372 exhibited a gradual increase in relative abundance with depth (Fig. 3). In addition to the more
11
12 373 prevalent taxa there were several families that appeared to a lesser extent only at depth and
13
14 374 included the photoheterotrophic Gemmatimonadetes, purple non-sulfur bacteria
15
16 375 Rhodobiaceae, and nitrite-oxidizing Nitrospiraceae. Detailed taxonomic profiles of Zone 2
17
18 376 and 3 are depicted as krona plots in Supplementary Figs. S4 and S5.

20
21 377 In addition to analysis of the bacterial composition, a beta diversity analysis was
22
23 378 completed to assess whether these observed taxonomic differences were statistically
24
25 379 significant. Unweighted UniFrac distance matrices were generated for the Bacteria amplicon
26
27 380 libraries and visualized using a jackknifed principal coordinate analysis (PCoA; Fig. 4A).
28
29 381 The results revealed that each of the three spatial zones represented distinctive microbial
30
31 382 communities with low standard deviation amongst the library replicates. Zones 2 and 3
32
33 383 shared a higher level of similarity with 27% of the variation between the upper and lower two
34
35 384 zones being explained by depth ($p=0.001$; $R^2=0.402$, adonis; Fig. 4A).
36
37
38
39

40 385

41 386 3.3. Phylogenetic composition of Archaea in thrombolite communities with depth

42
43 387 With regard to the overall archaeal diversity (e.g., Shannon Index) there was little difference
44
45 388 between the three zones with the recovered OTUs ranging from 506 to 671 (Table 1;
46
47 389 Supplementary Fig. S1B). Of the three recovered phyla, the Thaumarchaeota were dominant
48
49 390 in all three zones of the thrombolite forming mats with most of the reads sharing similarity to
50
51 391 the ammonia-oxidizing family Cenarchaeaceae (Fig. 5), specifically the genus
52
53 392 *Nitrosopumilus*. There were, however, some taxonomic differences between the different
54
55 393 spatial regions in the thrombolites. For example, phototrophic Halobacteriales showed the
56
57
58
59
60

1
2
3 394 highest abundance in the upper oxic Zone 1, as did the ammonia-oxidizer Nitrososphaeraceae
4
5 395 (Fig. 5). Although few methanogenic archaea taxa were detected in each of the three zones
6
7 396 they had the highest representation in the transitional Zone 2 with most of the reads sharing
8
9
10 397 similarity to the class Thermoplasmata and the family Methanocarcinaceae (Fig. 5). A beta
11
12 398 diversity test was also completed for the archaeal libraries and showed increased statistical
13
14 399 variation between replicates (Fig. 4B). Although the correlation was not as strong as in the
15
16 400 Bacteria, the three zones did appear to have spatially distinct Archaea populations with
17
18 401 approximately 20% of the variation between the zones being associated with depth ($p=0.017$;
19
20 402 $R^2=0.307$, adonis; Fig. 4B).
21
22

403

23
24
25 404 *3.4. Spatial profiling of functional gene complexity of thrombolite-forming mats using*
26
27 405 *predictive sequencing analysis*
28

29
30 406 In addition to profiling the microbial diversity within the thrombolite button mat, a
31
32 407 reconstruction of the functional gene complexity was generated for each zone using the 16S
33
34 408 rRNA gene sequences and the algorithm Phylogenetic Investigation of Communities by
35
36 409 Reconstruction of Unobserved States (PICRUSt; Langille *et al.*, 2013). As the number of
37
38 410 available reference genomes has steadily increased, PICRUSt has emerged as an effective
39
40 411 tool to accurately predict the functional complexity of the metagenomes based on taxonomic
41
42 412 information (Langille *et al.*, 2013). The tool has successfully been used to reconstruct the
43
44 413 metagenomes of a wide range of ecosystems including nonlithifying microbial mats and
45
46 414 stromatolites (Langille *et al.*, 2013; Casaburi *et al.*, 2016). A predicted metagenome was
47
48 415 generated for each spatial zone using the QIIME taxonomic output, which was then
49
50 416 statistically compared to a previously published metagenome of the entire button mat (0 – 9
51
52 417 mm; Mobberley *et al.*, 2013) to determine whether differences in the metabolic capabilities
53
54 418 could be observed between zones. The previously sequenced thrombolite metagenome was
55
56
57
58
59
60

1
2
3 419 re-annotated using MetaCV to update the metagenomic dataset and enabling comparable
4
5 420 annotations to the PICRUSt predictive metagenomes.
6

7 421 A total of 272 Kyoto Encyclopedia of Genes and Genomes (KEGG) functions were
8
9 422 identified in the three zones corresponding to 328 level 3 KEGG orthology (KO) entries,
10
11 423 which was consistent with the 268 KEGG functions observed in the re-annotated whole-mat
12
13 424 metagenome (Supplemental Table S2). Additionally, there was a strong correlation between
14
15 425 the PICRUSt predictive metagenomes and the whole mat metagenome ($r = 0.93$, Pearson),
16
17 426 with most of the KOs ($n = 222$) showing little or no variation between zones (Supplemental
18
19 427 Table S2). Of the 59 KOs that did show variation ($> 0.1\%$) several of the differences
20
21 428 occurred between the upper oxic Zone 1 and the two deeper Zones 2 and 3 (Fig. 6). In Zone
22
23 429 1, there was an increase in the relative abundance of KO pathways associated with
24
25 430 photosynthesis including the antennae proteins, porphyrin and chlorophyll metabolism,
26
27 431 whereas there was a lower abundance of genes associated with carboxylic acid metabolism
28
29 432 (e.g., butanoate, benzoate, caprolactam metabolism; Fig. 6). Deeper within the mat in Zones
30
31 433 2 and 3 there was a higher relative abundance of genes associated with fatty acid metabolism
32
33 434 and lipopolysaccharide biosynthesis compared to Zone 1. Despite these few select differences
34
35 435 many of highly represented pathways in the thrombolite-forming mats, such as DNA repair
36
37 436 proteins, two-component signaling, and bacterial motility, showed no differences between the
38
39 437 three spatial zones and likely reflect the core metabolisms associated with the thrombolite
40
41 438 microbiome.
42
43 439

440 3.5. Stable isotope analyses of thrombolitic carbonates

441 The calcified carbonate filaments associated with the *Dichothrix* cyanobacteria in the
442 upper Zone 1 were examined using a combined bulk isotopic analysis and targeted SIMS
443 approach coupled, which enabled an *in situ* high-spatial resolution analysis (Valley and Kita

1
2
3 444 2009; Kozdon *et al.*, 2009; Kita *et al.*, 2011) (Fig. 7). Bulk samples of dissected calcified
4
5 445 filaments had $\delta^{18}\text{O}$ values with a mean of $-0.53 \pm 0.06\text{‰}$ VPDB suggesting that the
6
7
8 446 precipitates associated with the filaments were not the result of evaporation, which would
9
10 447 cause an enrichment in heavy isotopes. Bulk $\delta^{13}\text{C}_{\text{carb}}$ values of the dissected filaments had a
11
12 448 mean of $4.98 \pm 0.03\text{‰}$, which was similar to the surrounding carbonate sediments ($+4.06\text{‰}$
13
14 449 to $+4.94\text{‰}$; mean = $4.64 \pm 0.30\text{‰}$). The $\delta^{13}\text{C}$ values for the organic matter associated with
15
16 450 the filaments was depleted compared to the sediment with values ranging -9.87‰ and -
17
18 451 9.22‰ (mean = $-9.64 \pm 0.24\text{‰}$), suggesting a relatively muted fractionation during organic
19
20 452 mater uptake, similar to what has been produced in other modern microbial mats (Canfield
21
22 453 and DesMarais, 1993). The $\delta^{15}\text{N}_{\text{org}}$ values associated with the filaments ranged from -1.09‰
23
24 454 to -0.14‰ (mean = $-0.79 \pm 0.29\text{‰}$), suggesting nitrogen fixation is a predominant means of
25
26 455 N assimilation (Sigman *et al.*, 2009) within the thrombolite-forming mats and correlates with
27
28 456 the high number of recovered diazotrophic Cyanobacteria and Alphaproteobacteria from the
29
30 457 mats.
31
32
33

34
35 458 To complement the bulk stable isotope analyses, the calcified filaments were also
36
37 459 analyzed *in situ* with SIMS to provide a higher spatial resolution (10 μm spot size) of the
38
39 460 $\delta^{18}\text{O}$ and $\delta^{13}\text{C}$ compositions of the calcified filaments. Micrographs depicting the SIMS target
40
41 461 sites along the filaments and associated carbonate precipitate are shown in Fig. 8. The $\delta^{18}\text{O}$
42
43 462 value of the surrounding carbonate sediments ranged from -2.0‰ and -0.6‰ (mean = $-1.26 \pm$
44
45 463 0.52‰), whereas the filaments exhibited a more depleted oxygen signature ranging from -
46
47 464 7.7‰ and -2.0‰ (mean = $-3.15 \pm 1.05\text{‰}$) (Fig. 7). The $\delta^{13}\text{C}$ values of the surrounding
48
49 465 sediments in the thrombolite button mats had a narrow range of values ($+3.6\text{‰}$ to $+4.6\text{‰}$;
50
51 466 mean = $4.10 \pm 0.42\text{‰}$), whereas the filaments had a much more dynamic range ($+0.10\text{‰}$ to
52
53 467 $+5.5\text{‰}$; mean = $2.7 \pm 1.25\text{‰}$). All stable isotope measurements are presented in order of
54
55 468 analysis in supplementary Tables S4-S5.
56
57
58
59
60

1
2
3 4694
5 470 **4. Discussion**

6
7 471 Within the thrombolite-forming mats of Highborne Cay the results of this study provide
8
9 472 evidence that: (1) despite the unlaminated microstructure discrete spatial zones of microbial
10
11 473 and biogeochemical signatures were present; (2) predictive metagenome reconstruction using
12
13 474 PICRUSt suggests a strong correlation between taxa and function, thereby identifying key
14
15 475 metabolic capabilities associated with carbonate precipitation; and (3) stable isotopic analysis
16
17 476 suggests that photosynthesis may be inducing precipitation in the thrombolite forming mats.
18
19

20
21 47722
23 478 *4.1. Microbial diversity within thrombolite-forming mats are highly structured*

24
25 479 The presence of discrete spatial zones of microbial and biochemical activity have
26
27 480 been well documented in stromatolites (e.g., Canfield and DesMarais, 1993; Visscher *et al.*,
28
29 481 1998; Wong *et al.*, 2015), however, the occurrence of similar zonation in mats that form
30
31 482 clotted thrombolites has only been recently suggested (Mobberley *et al.*, 2015). In this study,
32
33 483 analysis of the bacterial and archaeal communities revealed significantly different profiles of
34
35 484 taxa with depth (Fig. 4) suggesting the microbes form discrete microenvironments within the
36
37 485 thrombolite-forming mats with each zone having a potentially distinctive role in nutrient
38
39 486 cycling.
40
41

42
43 487 In the upper oxic Zone 1 the dominance of cyanobacterial sequences with similarity
44
45 488 to the filamentous Rivulariaceae reinforces the morphological observation that *Dichothrix*
46
47 489 sp., a member of the Rivulariaceae, serves as a ‘hot spot’ for photosynthetic activity and
48
49 490 carbonate deposition within the thick EPS matrix associated with the filaments (Planavsky *et*
50
51 491 *al.*, 2009). Sequencing of the *Dichothrix* sp. genome is underway (Louyakis and Foster
52
53 492 unpublished) and will help to expand the relatively small database of filamentous,
54
55 493 heterocystous cyanobacteria as well delineate the specific pathways associated with EPS
56
57
58
59
60

1
2
3 494 production in this keystone organism. In addition to the cyanobacteria, taxonomic analyses
4
5 495 also revealed an enrichment of diazotrophic, photoheterotrophs primarily associated with the
6
7 496 Rhodobacterales, Rhodospirillales, and Rhizobiales increasing with depth (Fig. 3). These
8
9
10 497 metabolically flexible Alphaproteobacteria are ubiquitous in marine microbial communities
11
12 498 including all previously characterized microbialites, coral symbioses, and sediments (e.g.,
13
14 499 Dang *et al.*, 2013; Houghton *et al.*, 2014; Wong *et al.*, 2015; Casaburi *et al.*, 2016; Hester *et*
15
16 500 *al.*, 2016; Suosaari *et al.*, 2016) and may be contributing to the carbon fixation rates deeper
17
18 501 within the thrombolitic mats where there are fewer cyanobacteria due to the reduced light
19
20 502 levels and the presence of sulfide. Additionally, the diazotrophic photoheterotrophs may be
21
22 503 helping to maintain the bioavailability of nitrogen in the thrombolite-forming communities.
23
24

25 504 Another key microbial functional group enriched within the thrombolite-forming
26
27 505 communities was sulfate-reducing bacteria (SRB), whose activity has been directly correlated
28
29 506 to deposition of carbonate in actively accreting stromatolites (Visscher *et al.*, 2000; Decho *et*
30
31 507 *al.*, 2010). There was a pronounced vertical stratification of SRBs in the thrombolite-forming
32
33 508 communities. Taxa associated with Desulfovibrionaceae, were enriched in the upper oxic
34
35 509 Zone 1, whereas the Deltasulfobacteraceae increased in their relative abundance with depth.
36
37 510 This vertical stratification of SRBs has been seen in the non-lithifying hypersaline mats of
38
39 511 Guerrero Negro, Mexico (Risatti *et al.*, 1994) and Solar Lake Egypt (Minz *et al.*, 1999).
40
41 512 Several species of sulfate-reducing Delsulfovribionaceae (e.g., *Desulfovibrio* spp. and
42
43 513 *Desulfomicrobium* spp) have been shown to be prevalent in the oxic zone of microbial mats
44
45 514 (Krekeler *et al.*, 1997) and high levels of sulfate reduction activity have been recorded in the
46
47 515 upper oxic zone of non-lithifying and stromatolite-forming mats (e.g., Canfield and
48
49 516 DesMarais, 1991; Visscher *et al.*, 1992, 2000). The abundance of SRBs in the oxic zone may
50
51 517 be, in part, due to the presence of sulfide oxidizing bacteria (SOBs). There was an enrichment
52
53 518 of the families Thiotrichaceae and Chromatiaceae in the upper Zone 1, which are known to
54
55
56
57
58
59
60

1
2
3 519 harbor many sulfide-oxidizing taxa (Pfennig and Trüper, 1992; Lenk *et al.*, 2011). The SOB
4
5 520 may be removing the O₂ and S²⁻ generated by the cyanobacteria and SRBs, both of which can
6
7 521 be toxic to the SRBs at high enough levels (Decho *et al.*, 2010). Together, this enrichment of
8
9
10 522 SOB, oxygen-tolerant SRBs and their vertical stratification in the thrombolite-forming may
11
12 523 suggest that, much like in the stromatolites, these different phylogenetic groups may be
13
14 524 playing distinctive community functions in response to variable carbon and electron donor
15
16 525 availability at different depths as well as the diel flux of oxygen and sulfide.
17

18
19 526 In addition to the bacteria, the archaeal population also exhibited stratification of
20
21 527 certain taxa within the thrombolite-forming mat. There was an enrichment of Halobacteriales
22
23 528 in the upper oxic Zone 1 of the thrombolitic mats. Members of this order are typically
24
25 529 chemoheterotrophic and can grow on a wide range sugars, carboxylic acids, alcohols and
26
27 530 amino acids. This aerobic taxon has been observed in both lithifying and nonlithifying
28
29 531 microbial mat communities primarily in hypersaline environments (Burns *et al.*, 2004; Arp *et*
30
31 532 *al.*, 2012; Schneider *et al.*, 2013) and may be contributing to the heterotrophic degradation of
32
33 533 EPS material associated with the calcified filaments. It should be noted that the salinity of the
34
35 534 porewater in the upper part of the microbialites increases significantly (~135 PSU; Visscher
36
37 535 unpubl) upon exposure to the atmosphere during low tide, creating temporary hypersaline
38
39 536 conditions.
40
41

42
43 537 Relatively few sequences were recovered from methanogenic archaea and these were
44
45 538 primarily associated with the Methanocarcinaceae. These taxonomic results correspond to
46
47 539 recovered methyltransferase-encoding genes in the thrombolite metagenome (Mobberley *et*
48
49 540 *al.*, 2013), and there was a slight enrichment of recovered sequences from Zone 2 (Fig. 5).
50
51 541 Members of the Methanocarcinaceae can undergo methanogenesis using CO₂, acetate, and C₁
52
53 542 compounds (Feist *et al.*, 2006) and have been shown to elevate pH levels in mat communities
54
55 543 via CO₂ consumption (Kenward *et al.*, 2009). However, the low levels of recovered taxa in
56
57
58
59
60

1
2
3 544 this study coupled with relatively few functional genes observed in the thrombolite
4
5 545 metagenome (Mobberley *et al.*, 2013) suggest that methanogenesis may be playing only a
6
7 546 minor role in promoting an alkaline environment within these thrombolitic mats.
8
9

10 547

11 548 *4.2. Predictive metagenome reconstruction shows strong correlation with taxa and function.*

12
13
14 549 The PICRUSt predictive metagenome strongly correlated ($r = 0.93$) with the
15
16 550 previously published whole shotgun library (Mobberley *et al.*, 2013) providing further
17
18 551 evidence that 16S rRNA gene libraries can be used to provide insight into the metabolic
19
20 552 capabilities of microbial ecosystems. There was extensive overlap in the relative abundance
21
22 553 of functional genes between the different depths in several pathways, such as nucleotide and
23
24 554 amino acid metabolism, genetic information processing, and environmental information
25
26 555 responses with the shotgun sequence library suggesting there is a core metagenome in the
27
28 556 thrombolite-forming mats at all depths (Fig. 6). Additionally, genes associated with several
29
30 557 key metabolisms associated with the promotion (e.g., photosynthesis, sulfate reduction) and
31
32 558 dissolution (e.g., sulfide oxidation, fermentation, ammonia oxidation) of carbonate
33
34 559 precipitation were observed within the thrombolite-forming mats.
35
36
37

38 560 Despite the extensive overlap between the core metagenome at each depth, some
39
40 561 differences were observed between the mat zones. The enrichment of genes associated with
41
42 562 photosynthesis pathways in the upper Zone 1 and the increase of genes associated with
43
44 563 different carboxylic and fatty acid metabolisms deeper within the mat reveal distinctive
45
46 564 metabolic transitions throughout the mat profile. These spatial differences in metabolic
47
48 565 capabilities are also reflected in the biochemical gradients observed within the mats (Fig. 1).
49
50 566 These functional genes could serve as ideal targets to examine the potential regulation of
51
52 567 these metabolisms within the thrombolite ecosystems potentially providing insight into the
53
54 568 molecular response to changing environmental variables, such as pH, oxygen and sulfide.
55
56
57
58
59
60

1
2
3 569 Additionally, by tracking these specific molecular pathways it may be possible elucidate the
4
5 570 specific genes and taxa involved in the diagenetic alteration of organic material in the
6
7 571 thrombolites over both spatial and temporal scales.
8

9
10 572

11 573 *4.3. Stable isotope profiling suggests photosynthesis is the major driver in thrombolite-*
12
13 *forming mats.*
14

15 575 In addition to the microbial and functional gene analyses the stable isotope profiling
16
17 576 provided additional insights into the microbial nitrogen cycling and the mechanisms driving
18
19 577 carbonate precipitation. Organic N isotope values approached 0‰, indicating nitrogen
20
21 578 fixation was the dominant N source (Hoering and Ford, 1960; Minagawa and Wada, 1986;
22
23 579 Sigman *et al.*, 2009), which is consistent with the abundance of heterocystous cyanobacteria,
24
25 580 such as *Dichothrix* sp., and numerous nitrogen fixing anoxygenic phototrophs identified in
26
27 581 Zone 1 (Fig. 8). These results are also consistent with the high number of nitrogen fixation
28
29 582 genes (e.g., *nifD*, *nifH*, *nifK*) recovered from the metagenome and metatranscriptome of the
30
31 583 thrombolites (Mobberley *et al.*, 2015). Additionally, the enrichment of ammonia oxidizing
32
33 584 archaea within the mat coupled with the low numbers of nitrification genes observed in both
34
35 585 the predictive and whole shotgun libraries suggested that these chemolithotrophs may be
36
37 586 actively involved in the cycling of the fixed nitrogen within the thrombolite forming mats.
38
39
40
41

42 587 Analysis of $\delta^{18}\text{O}$ values using both bulk and SIMS analyses do not provide evidence
43
44 588 of an evaporative signal and are suggestive of biologically induced precipitation. The high
45
46 589 rates of photosynthesis within the thrombolite-forming mats (Myshrall *et al.*, 2010) coupled
47
48 590 with the previously published observations that red algae distributed throughout the tufts of
49
50 591 *Dichothrix* sp. filaments lack precipitates (Planavsky *et al.*, 2009) make it unlikely that non-
51
52 592 biological processes, such as CO_2 degassing, are driving the precipitation within the
53
54 593 thrombolites. The SIMS $\delta^{18}\text{O}$ values for filaments are highly depleted compared to the values
55
56
57
58
59
60

1
2
3 594 associated with the sediments and previous studies have shown that increased ^{18}O depletion
4
5 595 under elevated pH (Spero and Lea, 1996) suggestive of rapid rates of carbonate precipitation
6
7 596 (McConnaughey, 1989). Although the offset between the bulk and SIMS $\delta^{18}\text{O}$ values cannot
8
9
10 597 yet be fully explained, systematically lower SIMS values have been observed up to 2‰
11
12 598 (Orland *et al.*, 2015) and may be the product of water or organics within the sample site.
13
14 599 Furthermore, the low variability in the $^{16}\text{OH}/^{16}\text{O}$ values (Supplemental Table S4) suggests
15
16 600 that the zonation revealed by the SIMS data is accurate. The difference between SIMS and
17
18 601 bulk measurements may, in part, reflect the extensive grinding during sample preparation for
19
20 602 bulk isotope analysis. Previous studies in corals have shown that the friction generated during
21
22 603 milling or drilling of the carbonate samples can cause inversion of aragonite to calcite (Waite
23
24 604 and Swart, 2015). As a result of extensive processing (e.g. milling), the $\delta^{18}\text{O}$ values cause
25
26 605 correction errors from 0.2 ‰ per 1% of inversion from aragonite to calcite (Waite and Swart,
27
28 606 2015). Such differences between the two approaches reinforce the value of using a SIMS-
29
30 607 based approach to capture the extensive variability that likely exists within the
31
32 608 microenvironments of thrombolite forming mats.

33
34
35
36 609 The bulk $\delta^{13}\text{C}$ values of the organic matter associated within the thrombolites were
37
38 610 heavy (mean $-9.64 \pm 0.24\text{‰}$) relative to RuBisCO-mediated carbon fixation, which exhibits
39
40 611 fractionations that typically span between -35 to -23‰ in both plant and microbial
41
42 612 ecosystems and can be highly species-dependent (Farquhar *et al.*, 1989; Falkowski, 1991).
43
44 613 These $\delta^{13}\text{C}$ –enriched values likely reflect diffusion limitations of CO_2 into the thrombolite-
45
46 614 forming mats. Similar values have been observed in microbial mats found in the hypersaline
47
48 615 Solar Lake ($-5.7 \pm 1.4\text{‰}$) and Gavish Sabkha ($-10 \pm 2.6\text{‰}$) and have been attributed to EPS-
49
50 616 rich materials on the surface of mats that impede transport of CO_2 into the mats (Schidlowski
51
52 617 *et al.*, 1984). Previous studies have also shown that external factors, such as increased salinity
53
54 618 and temperature, can also decrease the solubility of CO_2 (Mucci, 1983). Therefore, the
55
56
57
58
59
60

1
2
3 619 abundance of EPS material within the thrombolite-forming mats coupled with high rates of
4
5 620 productivity (Myshrall *et al.*, 2010) may result in a potential shortage of CO₂ that may reduce
6
7 621 isotopic discrimination of ¹³C and is consistent with the idea of CO₂ driving a pH shift and
8
9
10 622 inducing carbonate precipitation.

11
12 623 The overall carbon isotope profiles of the carbonate suggest that the thrombolites of
13
14 624 Highborne Cay are primarily the result of photoautotrophic carbon fixation. The bulk isotope
15
16 625 data for carbonates correlates well with previous analyses on the calcified filaments
17
18 626 (Planavsky *et al.*, 2009) and are slightly higher than the δ¹³C values of the adjacent
19
20 627 stromatolites, which have been suggested to be the product of heterotrophic processes
21
22 628 (Andres *et al.*, 2006). The SIMS values, however, are more variable than the bulk isotopes,
23
24 629 although the means are not statistically different. The extensive variability in the SIMS
25
26 630 δ¹³C_{carb} values for filaments may reflect CO₂ constraints in the microenvironments along the
27
28 631 vertically orientated cyanobacteria filaments. High rates of photosynthesis can deplete local
29
30 632 CO₂ concentrations resulting in variable fractionation rates (Calder and Parker, 1973).

31
32
33
34 633 Additionally, the lightest SIMS δ¹³C values in filaments may reflect the presence of
35
36 634 localized organics (e.g., EPS material) associated with the calcified filaments, given that
37
38 635 organic carbon has higher ionization efficiency than carbonate. However, as SIMS threshold
39
40 636 cutoffs were applied to eliminate any spots that might include organics, the lower δ¹³C
41
42 637 values likely accurately capture filament carbonate values. In contrast, the isotopically
43
44 638 enriched samples, relative to values predicted from precipitation from local marine DIC,
45
46 639 provides evidence for carbonate precipitation in a microenvironment influenced by carbon
47
48 640 dioxide uptake, which increases the pH (Visscher *et al.*, 1991, 1998, 2005; Planavsky *et al.*,
49
50 641 2009). The highest SIMS δ¹³C values are more isotopically enriched than any previously
51
52 642 reported Highborne Cay bulk thrombolite or filament δ¹³C values (Planavsky *et al.*, 2009).
53
54 643 Planavsky and others (2009) used an offset between *Dichothrix* filament and detrital
55
56
57
58
59
60

1
2
3 644 sediment $\delta^{13}\text{C}$ values to argue for photosynthetic carbon dioxide consumption as the
4
5 645 initiation factor for carbonate precipitation within the filament sheaths. The observed
6
7 646 markedly enriched filament $\delta^{13}\text{C}$ values strengthen the case for photosynthetic carbonate
8
9
10 647 precipitation trigger.

11 648

14 649 **5. Conclusions**

16 650 The integrated approaches of microbial diversity, metagenome reconstruction,
17
18 651 microelectrode, and stable isotope analysis provide a spatial portrait of thrombolite-forming
19
20 652 communities revealing that despite the unlaminated, clotted microstructures these
21
22 653 thrombotic communities form distinct taxonomic and metabolic stratifications. The results
23
24 654 of this study also reveal that the taxa and primary metabolic triggers associated with
25
26 655 precipitation in thrombolites are distinctive from stromatolites. Even within the same
27
28 656 ecosystem, where thrombolites are juxtaposed to stromatolites under similar environmental
29
30 657 conditions (e.g., pH, salinity, temperature, UV flux) these differences between their taxa and
31
32 658 metabolic activities appear to generate very distinct carbonate microstructures. Elucidating
33
34 659 how these disparate structural fabrics arise will require a more detailed look into the
35
36 660 networking and connectivity of the microbial interactions and metabolisms. Regulation of
37
38 661 these processes on both diel and seasonal time scales will help assess the patterns associated
39
40 662 with microbial activities and their response to their changing environment. Together, these
41
42 663 analyses help elucidate the pathways associated with microbialite formation and represent a
43
44 664 valuable tool to help reconstruct the microbiological and environmental conditions of the
45
46 665 past.

47 666

54 667 **Acknowledgements**

1
2
3 668 The authors would like to thank Jennifer Larimore for her technical assistance. A.S.L was
4
5 669 supported by the NSF Graduate Research Fellowship Program and J.M.M was supported by
6
7 670 the NASA Graduate Student Research Program fellowship (NNX10AO18H). The research
8
9 671 efforts were supported by the NASA Exobiology and Evolutionary Biology program element
10
11 672 (NNX12AD64G). WiscSIMS is funded by NSF (EAR1355590).
12
13
14
15

673

674 **Author Disclosure Statement**

675 No competing financial interests exist

676

677 **Author Contributions**

678 A.L., J.M., R.R., P.V., and J.F. conceived the experiments. J.M., P.H., J.F., and P.V.
679 collected the samples. All authors contributed to the performance and analysis of the
680 experiments. All authors reviewed and approved the final manuscript.

681

682 **References**

- 683 Aitken JD. (1967) Classification and environmental significance of cryptalgal limestones and
684 dolomites, with illustrations from the Cambrian and Ordovician of southwestern
685 Alberta. *Journal of Sedimentary Petrology*, 37, 1163-1178.
- 686 Andres M, Sumner D, Reid RP, and Swart PK. (2006) Isotopic fingerprints of microbial
687 respiration in aragonite from Bahamian stromatolites. *Geology*, 34, 973-976.
- 688 Andres MS, and Reid RP. (2006) Growth morphologies of modern marine stromatolites: a
689 case study from Highborne Cay, Bahamas. *Sedimentary Geology*, 185, 319-328.
- 690 Arp G, Helms G, Kalinska K, Schumann G, Reimer A, Reitner J, and Trichet J. (2012)
691 Photosynthesis versus exopolymer degradation in the formation of microbialites on

- 1
2
3 692 the atoll of Kiritimati, Republic of Kiribati, Central Pacific. *Geomicrobiology*
4
5 693 *Journal*, 29, 29-65.
6
7 694 Barns SM, Fundyga RE, Jeffries MW, and Pace NR. (1994) Remarkable archaeal diversity
8
9 695 detected in a Yellowstone National Park hot spring environment. *Proceedings of the*
10
11 696 *National Academy of Sciences*, 91, 1609-1613.
12
13 697 Bernhard JM, Edgcomb VP, Visscher PT, McIntyre-Wressnig A, Summons RE, Bouxsein
14
15 698 ML, Louis L, and Jeglinski M. (2013) Insights into foraminiferal influences on
16
17 699 microfabric of microbialites at Highborne Cay, Bahamas. *Proceedings of the*
18
19 700 *National Academy of Sciences*, 110, 9830-9834.
20
21
22 701 Bowlin EM, Klaus J, Foster JS, Andres M, Custals L, and Reid RP. (2012) Environmental
23
24 702 controls on microbial community cycling in modern marine stromatolites.
25
26 703 *Sedimentary Geology*, 263-264, 45-55.
27
28
29 704 Breitbart M, Hoare A, Nitti A, Siefert J, Haynes M, Dinsdale E, Edwards R, Souza V,
30
31 705 Rohwer F, and Hollander D. (2009) Metagenomic and stable isotopic analyses of
32
33 706 modern freshwater microbialites in Cuatro Ciénegas, Mexico. *Environmental*
34
35 707 *Microbiology*, 11, 16-34.
36
37
38 708 Burne RV, and Moore LS. (1987) Microbialites: organosedimentary deposits of benthic
39
40 709 microbial communities. *PALAIOS*, 2, 241-254.
41
42
43 710 Burns BP, Goh F, Allen M, and Neilan BA. (2004) Microbial diversity of extant stromatolites
44
45 711 in the hypersaline marine environment of Shark Bay, Australia. *Environmental*
46
47 712 *Microbiology*, 6, 1096-1101.
48
49
50 713 Calder JA, and Parker PL. (1973) Geochemical implications of induced changes in ¹³C
51
52 714 fractionation by blue-green algae. *Geochimica et Cosmochimica Acta*, 37, 133-140.
53
54
55 715 Canfield DE, and Des Marais DJ. (1991) Aerobic sulfate reduction in microbial mats.
56
57 716 *Science*, 251, 1471-1473.
58
59
60

- 1
2
3 717 Canfield DE, and Des Marais DJ. (1993) Biogeochemical cycles of carbon, sulfur, and free
4
5 718 oxygen in a microbial mat. *Geochimica et Cosmochimica Acta*, 57, 3971-3984.
6
7 719 Caporaso JG, Kuczynski J, Stombaugh J, Bittinger K, Bushman FD, Costello EK, Fierer N,
8
9 720 Pena AG, Goodrich JK, Gordon JI and others. (2010) QIIME allows analysis of high-
10
11 721 throughput community sequencing data. *Nature Methods*, 7, 335-336.
12
13 722 Casaburi G, Duscher AA, Reid RP, and Foster JS. (2016) Characterization of the stromatolite
14
15 723 microbiome from Little Darby Island, The Bahamas using predictive and whole
16
17 724 shotgun metagenomic analysis. *Environmental Microbiology*, 18: 1452-1469
18
19 725 Casamayor EO, Massana R, Benlloch S, Ovreas L, Diez B, Goddard VJ, Gasol JM, Joint I,
20
21 726 Rodriguez-Valera F, and Pedros-Alio C. (2002) Changes in archaeal, bacterial and
22
23 727 eukaryal assemblages along a salinity gradient by comparison of genetic
24
25 728 fingerprinting methods in a multipond solar saltern. *Environmental Microbiology*, 4,
26
27 729 338-48.
28
29 730 Dang H, Yang J, Li J, Luan X, Zhang Y, Gu G, Xue R, Zong M, and Klotz MG. (2013)
30
31 731 Environment-dependent distribution of the sediment nifH-harboring microbiota in the
32
33 732 Northern South China Sea. *Applied and Environmental Microbiology*, 79, 121-132.
34
35 733 Decho AW, Norman RS, and Visscher PT. (2010) Quorum sensing in natural environments:
36
37 734 emerging views from microbial mats. *Trends in Microbiology*, 18, 73-80.
38
39 735 DeLong EF. (1992) Archaea in coastal marine environments. *Proceedings of the National*
40
41 736 *Academy of Sciences*, 89, 5685-5689.
42
43 737 DeSantis TZ, Hugenholtz P, Larsen N, Rojas M, Brodie EL, Keller K, Huber T, Dalevi D, Hu
44
45 738 P, and Andersen GL. (2006) Greengenes, a chimera-checked 16S rRNA gene
46
47 739 database and workbench compatible with ARB. *Applied and Environmental*
48
49 740 *Microbiology*, 72, 5069-5072.
50
51 741 Dravis JJ. (1983) Hardened subtidal stromatolites, Bahamas. *Science*, 219, 385-386.
52
53
54
55
56
57
58
59
60

- 1
2
3 742 Dupraz C, Reid RP, Braissant O, Decho AW, Norman RS, and Visscher PT. (2009)
4
5 743 Processes of carbonate precipitation in modern microbial mats. *Earth Science*
6
7 744 *Reviews*, 96, 141-162.
8
9
10 745 Dupraz C, and Visscher PT. (2005) Microbial lithification in marine stromatolites and
11
12 746 hypersaline mats. *Trends in Microbiology*, 13, 429-438.
13
14 747 Dupraz C, Visscher PT, Baumgartner LK, and Reid RP. (2004) Microbe-mineral interactions:
15
16 748 early carbonate precipitation in a hypersaline lake (Eleuthera Island, Bahamas).
17
18 749 *Sedimentology*, 51, 1-21.
19
20
21 750 Edgcomb VP, Bernhard JM, Beaudoin D, Pruss S, Welander PV, Schubotz F, Mehay S,
22
23 751 Gillespie AL, and Summons RE. (2013) Molecular indicators of microbial diversity
24
25 752 in oolitic sands of Highborne Cay, Bahamas. *Geobiology*, 11, 234-251.
26
27 753 Falkowski PG. (1991) Species variability in the fractionation of ^{13}C and ^{12}C by marine
28
29 754 phytoplankton. *Journal of Plankton Research*, 13, 21-28.
30
31
32 755 Farquhar GD, Ehleringer JR, and Hubick KT. (1989) Carbon isotope discrimination and
33
34 756 photosynthesis. *Annual Review of Plant Physiology and Plant Molecular Biology*, 40,
35
36 757 503-537.
37
38 758 Feist AM, Scholten JC, Palsson BO, Brockman FJ, and Ideker T. (2006) Modeling
39
40 759 methanogenesis with a genome-scale metabolic reconstruction of *Methanosarcina*
41
42 760 *barkeri*. *Molecular System Biology*, 2, 1.
43
44
45 761 Foster JS, and Green SJ. (2011) Microbial diversity in modern stromatolites In: *Cellular*
46
47 762 *Origin, Life in Extreme Habitats and Astrobiology: Interactions with Sediments*.
48
49 763 edited by J Seckbach and V Tewaris, Springer, p 385-405.
50
51
52 764 Gallagher KL, Kading TJ, Braissant O, Dupraz C, and Visscher PT. (2012) Inside the
53
54 765 alkalinity engine: The role of electron donors in the organomineralization potential of
55
56 766 sulfate-reducing bacteria. *Geobiology*, 10, 518-530.
57
58
59
60

- 1
2
3 767 Glunk C, Dupraz C, Braissant O, Gallagher KL, Verrecchia EP, and Visscher PT. (2011)
4
5 768 Microbially mediated carbonate precipitation in a hypersaline lake, Big Pond (Elutera,
6
7 769 Bahamas). *Sedimentology*, 58, 720-738.
8
9
10 770 Hester ER, Barott KL, Nulton J, Vermeij NJA, and Rohwer FL. (2016) Stable and sporadic
11
12 771 symbiotic communities of coral and algal holobionts. *ISME Journal*, 10, 1157-1169.
13
14 772 Hoering T, and Ford HT. (1960) The isotope effect in the fixation of nitrogen by *Azotobacter*.
15
16 773 *Journal of American Chemical Society*, 82, 376-378.
17
18 774 Houghton J, Fike D, Druschel G, Orphan V, Hoehler TM, and Des Marais DJ. (2014) Spatial
19
20 775 variability in photosynthetic and heterotrophic activity drives localized delta13C org
21
22 776 fluctuations and carbonate precipitation in hypersaline microbial mats. *Geobiology*,
23
24 777 12, 557-574.
25
26
27 778 Huson DH, Auch AF, Qi J, and Schuster SC. (2007) MEGAN analysis of metagenomic data.
28
29 779 *Genome Research*, 17, 377-386.
30
31
32 780 Kanehisa M, and Goto S. (2000) KEGG: kyoto encyclopedia of genes and genomes. *Nucleic*
33
34 781 *Acids Research*, 28, 27-30.
35
36 782 Kennard JM, and James NP. (1986) Thrombolites and stromatolites: two distinct types of
37
38 783 microbial structures. *PALAIOS*, 1, 492-503.
39
40 784 Kenward PA, Goldstein RH, Gonzalez LA, and Roberts JA. (2009) Precipitation of low-
41
42 785 temperature dolomite from an anaerobic microbial consortium: the role of
43
44 786 methanogenic Archaea. *Geobiology*, 7, 556-565.
45
46
47 787 Khodadad CL, and Foster JS. (2012) Metagenomic and metabolic profiling of nonlithifying
48
49 788 and lithifying stromatolitic mats of Highborne Cay, The Bahamas. *PLoS ONE*, 7,
50
51 789 e38229.
52
53
54 790 Kita NT, Huberty JM, Kozdon R, Beard BL, and Valley JW. (2011) High-precision SIMS
55
56 791 oxygen, sulfur and iron stable isotope analyses of geological materials: accuracy,
57
58
59
60

- 1
2
3 792 surface topography and crystal orientation. *Surface and Interface Analysis*, 43, 427-
4
5 793 431.
6
7 794 Kozdon R, Kelly DC, Kita NT, Fournelle JH, and Valley JW. (2011) Planktonic
8
9 795 foraminiferal oxygen isotope analysis by ion microprobe technique suggests warm
10
11 796 tropical sea surface temperatures during the Early Paleogene. *Paleoceanography*, 26.
12
13 797 Kozdon R, Ushikubo T, Kita NT, Spicuzza M, and Valley JW. (2009) Intratest oxygen
14
15 798 isotope variability in the planktonic foraminifer *N. pachyderma*: real versus apparent
16
17 799 vital effects by ion microprobe. *Chemical Geology*, 258, 327-337.
20
21 800 Krekeler D, Teske AP, and Cypionka H. (1997) Strategies of sulfate-reducing bacteria to
22
23 801 escape oxygen stress in a cyanobacterial mat. *FEMS Microbiology Ecology*, 25, 89-
24
25 802 96.
26
27 803 Langille MG, Zaneveld J, Caporaso JG, McDonald D, Knights D, Reyes JA, Clemente JC,
28
29 804 Burkepille DE, Vega Thurber RL, Knight R and others. (2013) Predictive functional
30
31 805 profiling of microbial communities using 16S rRNA marker gene sequences. *Nature*
32
33 806 *Biotechnology*, 31, 814-821.
34
35
36 807 Laval B, Cady SL, Pollack JC, McKay CP, Bird JS, Grotzinger JP, Ford DC, and Bohm HR.
37
38 808 (2000) Modern freshwater microbialite analogues for ancient dendritic reef structures.
39
40 809 *Nature*, 407, 626-629.
41
42
43 810 Lenk S, Arnds J, Zerjatke K, Musat N, Amann R, and Musmann M. (2011) Novel groups of
44
45 811 Gammaproteobacteria catalyse sulfur oxidation and carbon fixation in a coastal,
46
47 812 intertidal sediment. *Environmental Microbiology*, 13, 758-774.
48
49
50 813 Linzmeier B, Kozdon R, Peters S, and Valley JW. (2016) Oxygen isotope variability within
51
52 814 growth bands suggests daily depth migration behavior is recorded in *Nautilus* shell
53
54 815 aragonite. *PLOS ONE*, e0153890.
55
56
57
58
59
60

- 1
2
3 816 Logan BW. (1961) *Cryptozoan* and associated stromatolites from the recent, Shark Bay,
4
5 817 Western Australia. *Journal of Geology*, 69, 517-533.
6
7 818 Lozupone C, and Knight R. (2005) UniFrac: a new phylogenetic method for comparing
8
9 819 microbial communities. *Applied and Environmental Microbiology*, 71, 8228-8235.
10
11 820 McConnaughey T. (1989) ^{13}C and ^{18}O isotopic disequilibrium in biological carbonates: I.
12
13 821 Patterns. *Geochimica et Cosmochimica Acta*, 53, 151-162.
14
15 822 Minagawa M, and Wada E. (1986) Nitrogen isotope ratios of red tide organisms in the East
16
17 823 China Sea: a characterization of biological nitrogen fixation. *Marine Chemistry*, 19,
18
19 824 245-259.
20
21 825 Minz D, Fishbain S, Green SJ, Muyzer G, Cohen Y, Rittmann BE, and Stahl DA. (1999)
22
23 826 Unexpected population distribution in a microbial mat community: sulfate-reducing
24
25 827 bacteria localized to the highly oxic chemocline in contrast to a eukaryotic preference
26
27 828 for anoxia. *Applied and Environmental Microbiology*, 65, 4659-4665.
28
29 829 Mobberley JM, Khodadad CL, and Foster JS. (2013) Metabolic potential of lithifying
30
31 830 cyanobacteria-dominated thrombolitic mats. *Photosynthesis Research*, 118, 125-140.
32
33 831 Mobberley JM, Khodadad CL, Visscher PT, Reid RP, Hagan P, and Foster JS. (2015) Inner
34
35 832 workings of thrombolites: spatial gradients of metabolic activity as revealed by
36
37 833 metatranscriptome profiling. *Scientific Reports*, 5, 12601.
38
39 834 Mobberley JM, Ortega MC, and Foster JS. (2012) Comparative microbial diversity analyses
40
41 835 of modern marine thrombolitic mats by barcoded pyrosequencing. *Environmental*
42
43 836 *Microbiology*, 14, 82-100.
44
45 837 Mucci A. (1983) The solubility of calcite and aragonite in seawater at various salinities,
46
47 838 temperatures, and one atmosphere total pressure. *American Journal of Science*, 283,
48
49 839 780-799.
50
51
52
53
54
55
56
57
58
59
60

- 1
2
3 840 Myshrall K, Mobberley JM, Green SJ, Visscher PT, Havemann SA, Reid RP, and Foster JS.
4
5 841 (2010) Biogeochemical cycling and microbial diversity in the modern marine
6
7 842 thrombolites of Highborne Cay, Bahamas. *Geobiology*, 8, 337-354.
8
9
10 843 Ondov BD, Bergman NH, and Phillippy AM. (2011) Interactive metagenomic visualization
11
12 844 in a Web browser. *BMC Bioinformatics*, 12, 385.
13
14 845 Orland IJ. (2012) Seasonality from speleothems: high-resolution ion microprobe studies at
15
16 846 Soreq Cave, Israel: University of Wisconsin-Madison.
17
18 847 Orland IJ, Bar-Matthews M, Kita NT, Ayalon A, Matthews A, and Valley JW. (2009)
19
20 848 Climate deterioration in the Eastern Mediterranean as revealed by ion microprobe
21
22 849 analysis of a speleothem that grew from 2.2 to 0.9 ka in Soreq Cave, Israel.
23
24 850 *Quaternary Research*, 71, 27-35.
25
26
27 851 Pages A, Welsh DT, Teasdale PR, Grice K, Vacher M, Bennett WW, and Visscher PT.
28
29 852 (2014) Diel fluctuations in solute distributions and biogeochemical cycling in a
30
31 853 hypersaline microbial mat from Shark Bay, WA. *Marine Chemistry*, 167, 102-112.
32
33
34 854 Paul VG, Wronkiewicz DJ, Mormile MR, and Foster JS. (2016) Mineralogy and microbial
35
36 855 diversity of the microbialites in the hypersaline Storr's Lake, The Bahamas.
37
38 856 *Astrobiology*, 16, 282-300.
39
40
41 857 Pfennig N, and Trüper HG. (1992) The family Chromatiaceae. In: *The Prokaryotes*, Springer,
42
43 858 New York, p 3200-3221.
44
45 859 Planavsky N, and Ginsburg RN. (2009) Taphonomy of modern marine Bahamian
46
47 860 microbialites. *PALAIOS*, 24, 5-17.
48
49 861 Planavsky N, Reid RP, Andres M, Visscher PT, Myshrall KL, and Lyons TW. (2009)
50
51 862 Formation and diagenesis of modern marine calcified cyanobacteria. *Geobiology*, 7,
52
53 863 566-576.
54
55
56
57
58
59
60

- 1
2
3 864 Price MN, Dehal PS, and Arkin AP. (2010) FastTree 2--approximately maximum-likelihood
4
5 865 trees for large alignments. *PLoS ONE*, 5, e9490.
6
7 866 Reid RP, Macintyre IG, and Steneck RS. (1999) A microbialite/algal-ridge fringing reef
8
9 867 complex, Highborne Cay, Bahamas. *Atoll Research Bulletin*, 465, 459-465.
10
11 868 Reid RP, Visscher PT, Decho AW, Stolz JF, Bebout BM, Dupraz C, Macintyre IG, Paerl
12
13 869 HW, Pinckney JL, Prufert-Bebout L and others. (2000) The role of microbes in
14
15 870 accretion, lamination and early lithification of modern marine stromatolites. *Nature*,
16
17 871 406, 989-992.
18
19 872 Risatti JB, Capman WC, and Stahl DA. (1994) Community structure of a microbial mat: the
20
21 873 phylogenetic dimension. *Proceedings of the National Academy of Sciences*, 91,
22
23 874 10173-10177.
24
25 875 Ruvindy R, White Iii RA, Neilan BA, and Burns BP. (2016) Unravelling core microbial
26
27 876 metabolisms in the hypersaline microbial mats of Shark Bay using high-throughput
28
29 877 metagenomics. *ISME Journal*, 10, 183-196.
30
31 878 Saghaï A, Zivanovic Y, Zeyen N, Moreira D, Benzerara K, Deschamps P, Bertolino P, Ragon
32
33 879 M, Tavera R, Lopez-Archilla AI and others. (2015) Metagenome-based diversity
34
35 880 analyses suggest a significant contribution of non-cyanobacterial lineages to
36
37 881 carbonate precipitation in modern microbialites. *Frontiers in Microbiology*, 6, 797.
38
39 882 Schidlowski M, and Matzigkeit U. (1984) Superheavy organic carbon from hypersaline
40
41 883 microbial mats. *Naturwissenschaften*, 71, 303-308.
42
43 884 Schneider D, Arp G, Reimer A, Reitner J, and Daniel R. (2013) Phylogenetic analysis of a
44
45 885 microbialite-forming microbial mat from a hypersaline lake of the Kiritimati atoll,
46
47 886 Central Pacific. *PLoS ONE*, 8, e66662.
48
49 887 Sigman DM, Karsh KL, and Casciotti KL. (2009) Ocean process tracers: nitrogen isotopes in
50
51 888 the ocean. *Encyclopedia of Ocean Science*, 4138-4153.
52
53
54
55
56
57
58
59
60

- 1
2
3 889 Spero HJ, and Lea DW. (1996) Experimental determination of stable isotope variability in
4
5 890 *Globigerina bulloides*: implications for paleoceanographic reconstructions. *Marine*
6
7 891 *Micropaleontology*, 28, 231-246.
- 8
9
10 892 Stolz JF, Reid RP, Visscher PT, Decho AW, Norman RS, Aspden RJ, Bowlin EM, Franks J,
11
12 893 Foster JS, Paterson DM and others. (2009) The microbial communities of the modern
13
14 894 marine stromatolites at Highborne Cay, Bahamas. *Atoll Research Bulletin*, 567, 1-29.
- 15
16 895 Suosaari EP, Reid RP, Playford PE, Foster JS, Stolz JF, Casaburi G, Hagan PD, Chirayath V,
17
18 896 Macintyre IG, Planavsky NJ and others. (2016) New multi-scale perspectives on the
19
20 897 stromatolites of Shark Bay, Western Australia. *Scientific Reports*, 6, 20557.
- 21
22
23 898 Valley JW, and Kita NT. (2009) In situ oxygen isotope geochemistry by ion microprobe. In:
24
25 899 *Mineralogical Association of Canada Short Course*, p 19-63.
- 26
27 900 Vazquez-Baeza Y, Pirrung M, Gonzalez A, and Knight R. (2013) EMPeror: a tool for
28
29 901 visualizing high-throughput microbial community data. *Gigascience*, 2, 16.
- 30
31
32 902 Vetter L, Kozdon R, Valley JW, Mora CI, and Spero HJ. (2014) SIMS measurements of
33
34 903 intrashell $\delta^{13}\text{C}$ in the cultured planktic foraminifer *Orbulina universa*. *Geochimica et*
35
36 904 *Cosmochimica Acta*, 139, 527-539.
- 37
38
39 905 Visscher PT, Beukema J, and van Gemerden H. (1991) In situ characterization of sediments:
40
41 906 measurement of oxygen and sulfide profiles with a novel combined needle electrode.
42
43 907 *Limnology and Oceanography*, 36, 1476-1480.
- 44
45
46 908 Visscher PT, Prins RA, and van Gemerden H. (1992) Rates of sulfate reduction and
47
48 909 thiosulfate consumption in a marine microbial mat. *FEMS Microbiology Letters*, 86,
49
50 910 283-293.
- 51
52 911 Visscher PT, Reid RP, and Bebout BM. (2000) Microscale observations of sulfate reduction:
53
54 912 correlation of microbial activity with lithified micritic laminae in modern marine
55
56 913 stromatolites. *Geology*, 28, 919-922.
- 57
58
59
60

- 1
2
3 914 Visscher PT, Reid RP, Bebout BM, Hoefft SE, Macintyre IG, and Thompson JA. (1998)
4
5 915 Formation of lithified micritic laminae in modern marine stromatolites (Bahamas):
6
7 916 The role of sulfur cycling. *American Mineralogist*, 83, 1482-1493.
8
9
10 917 Visscher PT, and Stolz JF. (2005) Microbial mats as bioreactors: populations, processes and
11
12 918 products. *Palaeogeography, Palaeoclimatology, Palaeoecology*, 219, 87-100.
13
14 919 Waite AJ, and Swart PK. (2015) The inversion of aragonite to calcite during the sampling of
15
16 920 skeletal archives: implications for proxy interpretation. *Rapid Communications in*
17
18 921 *Mass Spectrometry*, 29, 955-964.
19
20
21 922 Warden JG, Casaburi G, Omelon CR, Bennett PC, Breecker DO, and Foster JS. (2016)
22
23 923 Characterization of microbial mat microbiomes in the modern thrombolite ecosystem
24
25 924 of Lake Clifton, Western Australia using shotgun metagenomics. *Frontiers in*
26
27 925 *Microbiology*, doi: 10.3389/fmicb.2016.01064.
28
29
30 926 White RA, 3rd, Chan AM, Gavelis GS, Leander BS, Brady AL, Slater GF, Lim DS, and
31
32 927 Suttle CA. (2016) Metagenomic Analysis Suggests Modern Freshwater Microbialites
33
34 928 Harbor a Distinct Core Microbial Community. *Frontiers in Microbiology*, 6, 1531.
35
36 929 White RA, 3rd, Power IM, Dipple GM, Southam G, and Suttle CA. (2015) Metagenomic
37
38 930 analysis reveals that modern microbialites and polar microbial mats have similar
39
40 931 taxonomic and functional potential. *Frontiers in Microbiology*, 6, 966.
41
42
43 932 Wickham H. (2009) ggplot2: elegant graphics for data analysis. Springer Science & Business
44
45 933 Media.
46
47 934 Williford KH, Ushikubo T, Lepot K, Kitajima K, Hallmann C, Spicuzza MJ, Kozdon R,
48
49 935 Eigenbrode JL, Summons RE, and Valley JW. (2016) Carbon and sulfur isotopic
50
51 936 signatures of ancient life and environment at the microbial scale: Neoproterozoic shales
52
53
54 937 and carbonates. *Geobiology*, 14, 105-128.
55
56
57
58
59
60

1
2
3 938 Wong HL, Smith DL, Visscher PT, and Burns BP. (2015) Niche differentiation of bacterial
4
5 939 communities at a millimeter scale in Shark Bay microbial mats. *Scientific Reports*, 5,
6
7 940 15607.
8
9

10 941

11
12
13 942 **Figure Legends**

14
15 943 **FIG. 1.** The thrombolites of Highborne Cay, The Bahamas. **(A)** Intertidal thrombolite
16
17 944 platforms from Site 5. Bar, 1 m. **(B)** Light micrograph of a thrombolite forming button mat
18
19 945 revealing extensive vertical assemblages of calcified filaments (arrows). Bar, 500 μm . **(C)** *In*
20
21 946 *situ* depth profiles of oxygen (square), sulfide (triangle) and pH (circle) collected at peak of
22
23 947 photosynthesis (open symbols) or respiration (filled symbols). **(D)** Cross section of button
24
25 948 mat depicting the three spatial regions including an oxic Zone 1 (0 – 3 mm), transitional Zone
26
27 949 2 (3 – 5 mm), and anoxic Zone 3 (5 – 9 mm). Bar, 3 mm.
28
29

30 950

31
32
33 951 **FIG. 2.** Taxonomic distribution of cyanobacteria within the thrombolite-forming mats
34
35 952 derived from MEGAN5 using the Greengenes database. Read counts are presented
36
37 953 logarithmically depicting the distributions for Zone 1 (blue), Zone 2 (green), and Zone 3
38
39 954 (red). Read abundance data for each taxonomic level are included in parentheses.
40

41 955

42
43
44 956 **FIG. 3.** Taxonomic distribution of Bacteria within the thrombolite-forming mats derived
45
46 957 from MEGAN5 using the Greengenes database. Read counts are presented logarithmically
47
48 958 depicting the distributions for Zone 1 (blue), Zone 2 (green), and Zone 3 (red). Read
49
50 959 abundance data for each taxonomic level are included in parentheses.
51

52 960

53
54
55 961 **FIG. 4.** Comparison of diversity analyses of three spatial zone within the thrombolite-
56
57 962 forming mats. Principal coordinate analysis of communities from unweighted UniFrac
58
59
60

1
2
3 963 distance matrix of Zone 1 (0 – 3 mm, blue), Zone 2 (3 – 5 mm, green), and Zone 3 (5 – 9
4
5 964 mm, red) in (A) Bacteria and (B) Archaea populations. Ellipses represent standard deviation
6
7 965 over ten rarefaction samplings. Adonis tests suggest that depth is a significant predictor of
8
9 966 community composition for both bacterial ($R=0.402$, $p=0.001$) and archaeal ($R=0.307$,
10
11 967 $p=0.017$) communities.
12
13
14 968

15
16 969 **FIG. 5.** Taxonomic distribution of Archaea within the thrombolite-forming mats derived
17
18 970 from MEGAN5 using the Greengenes database. Read counts are presented logarithmically
19
20 971 depicting the distributions for Zone 1 (blue), Zone 2 (green), and Zone 3 (red). Read
21
22 972 abundance data for each taxonomic level are included in parentheses.
23
24
25 973

26
27 974 **FIG. 6.** Functional gene comparison of the three thrombolitic mat spatial zones from 16S
28
29 975 rRNA metabolic prediction (PICRUSt) and whole shotgun sequencing. Pearson correlation
30
31 976 value (r) is shown for the comparison of metabolic predictions for Zone 1 (blue), Zone 2
32
33 977 (green) and Zone 3 (red) and the whole mat shotgun metagenome.
34
35
36 978

37
38 979 **FIG 7.** Stable isotope results for calcified filaments located in the upper 3 mm of thrombolite
39
40 980 forming button mat. (A) Oxygen isotope values of organic and inorganic fractions using both
41
42 981 bulk and SIMS analysis. Analyses were completed for both background carbonate
43
44 982 precipitates (sediment), calcified filaments (filaments) and untreated whole mat samples. (B)
45
46 983 Carbon and nitrogen isotope values of both organic and inorganic fractions using both bulk
47
48 984 and secondary ion mass spectroscopy (SIMS) analysis. (C) Comparative plot of SIMS values
49
50 985 collected for oxygen and carbon isotopes. All results are expressed in delta notation with
51
52 986 respect to the carbon/oxygen Vienna Peedee Belemnite (VPDB) or nitrogen air (AIR)
53
54 987 standard.
55
56
57
58
59
60

1
2
3
4
5
6
7
8
9
10
11
12
13
14
15
16
17
18
19
20
21
22
23
24
25
26
27
28
29
30
31
32
33
34
35
36
37
38
39
40
41
42
43
44
45
46
47
48
49
50
51
52
53
54
55
56
57
58
59
60

988

989 **FIG. 8.** Overview of target areas for SIMS analyses within the thrombolite forming mat. **(A)**

990 Petrographic thin section of *Dichothrix* sp. filaments (f) and associated carbonate precipitate

991 (cp) surrounded by sediments such as ooids (o). **(B)** Gold-coated reflected light image as

992 viewed by the SIMS instrument. **(C)** SEM micrograph showing the numerous 6-10 μm pits

993 formed during the SIMS analysis. Boxes depict representative pits that show both high

994 (green) and low (red) quality targets within the sample. **(D)** Higher resolution SEM

995 micrograph of representative high quality pit (corresponding to green box in C) showing no

996 textural anomalies or cracks. **(E)** SEM micrograph of low quality pit (corresponding to red

997 box in C) showing crack within the targeted sample site. All low quality target sites were

998 removed from down-stream analyses.

999

1000 **Supplemental FIG. S1.** Rarefaction plots for number of observed species approaching

1001 asymptote at read cutoffs of **(A)** 3691 for Bacteria and **(B)** 3587 for Archaea. Error bars

1002 represent standard deviation of three biological replicates for Zone 1 (0 – 3 mm, blue), Zone

1003 2 (3 – 5 mm, green) and Zone 3 (5 – 9 mm, red).

1004

1005 **Supplemental FIG. S2.** Relative abundance of bacterial population. Lines depict family-

1006 level OTU (97% cutoff) differences between depth zones grouped by phylum. Taxonomy

1007 was assigned using the Greengenes database and filtered by abundance (0.005%).

1008

1009 **Supplemental FIG. S3.** Taxonomic abundance diversity of bacteria associated with Zone 1

1010 (0 - 3 mm) of the thrombolite forming mats as visualized in a hierarchal Krona plot. Each

1011 ring within the plot represents a different taxonomic level (i.e., phylum, class, order, family).

1012 Taxa comprising less than 0.1% of the community were omitted.

1
2
3 1013
4

5 1014 **Supplemental FIG. S4.** Taxonomic abundance diversity of bacteria associated with Zone 2
6
7 1015 (3 - 5 mm) of the thrombolites as visualized in a hierarchal Krona plot. Each ring within the
8
9 1016 plot represents a different taxonomic level (i.e., phylum, class, order, family). Taxa
10
11 1017 comprising less than 0.1% of the community were omitted.
12

13
14 1018

15
16 1019 **Supplemental FIG S5.** Taxonomic abundance diversity of bacteria associated with Zone 3
17
18 1020 (5 - 9 mm) of the thrombolites as visualized in a hierarchal Krona plot. Each ring within the
19
20 1021 plot represents a different taxonomic level (i.e., phylum, class, order, family). Taxa
21
22 1022 comprising less than 0.1% of the community were omitted.
23

24
25 1023

26
27 1024 **Supplementary Table S1.** Primer list used to generate titanium 454 barcoded libraries for
28
29 1025 bacteria and archaea.
30

31
32 1026

33
34 1027 **Supplemental Table S2.** Functional gene complexity of predicted and whole shotgun
35
36 1028 metagenome in the thrombolite forming mats of Highborne Cay, The Bahamas. (please note
37
38 1029 this table format is an excel worksheet but had to be uploaded as csv file).
39

40
41 1030

42
43 1031 **Supplemental Table S3.** Percent of key elements by weight found in the thrombolite-
44
45 1032 forming microbial mat.
46

47
48 1033

49
50 1034 **Supplemental Table S4:** Ion microprobe raw and corrected oxygen isotope ratios from 77
51
52 1035 analyses of thrombolite samples 10B1 and 10B2 from Highborne Cay, The Bahamas. (Please
53
54 1036 note this table format is excel worksheet but had to be uploaded as two page csv file).
55

56
57 1037
58
59
60

1
2
3 1038 **Supplemental Table S5:** Ion microprobe raw and corrected carbon isotope ratios from 92
4
5 1039 analyses of thrombolite samples 10B1 and 10B2 from Highborne Cay, The Bahamas. (Please
6
7 1040 note this table format is excel worksheet but had to be uploaded as two page pcsv file).
8
9
10 1041
11
12 1042
13
14 1043
15
16
17
18
19
20
21
22
23
24
25
26
27
28
29
30
31
32
33
34
35
36
37
38
39
40
41
42
43
44
45
46
47
48
49
50
51
52
53
54
55
56
57
58
59
60

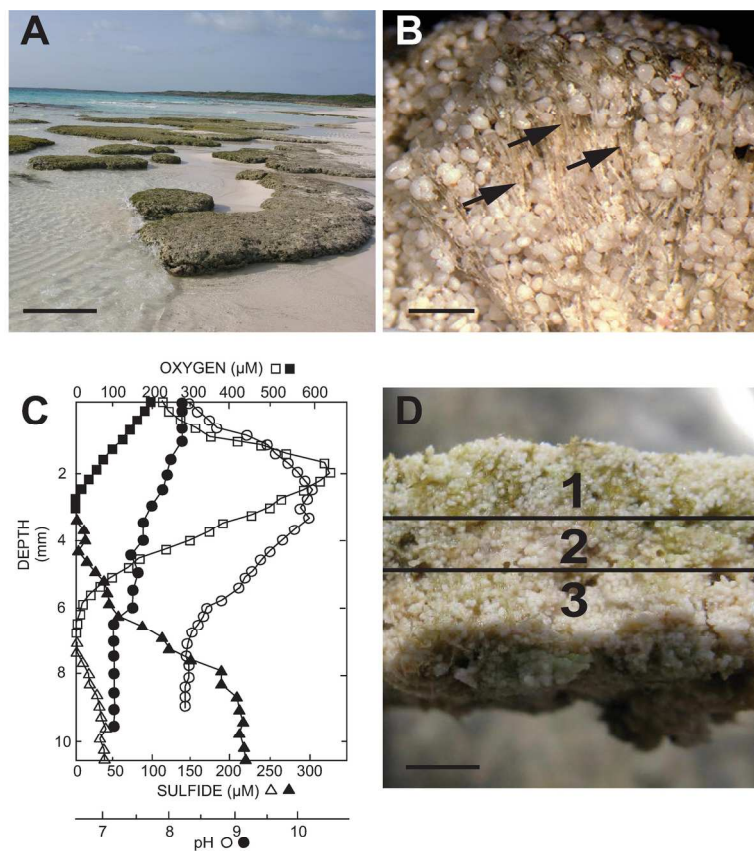


FIG. 1. The thrombolites of Highborne Cay, The Bahamas. (A) Intertidal thrombolite platforms from Site 5. Bar, 1 m. (B) Light micrograph of a thrombolite forming button mat revealing extensive vertical assemblages of calcified filaments (arrows). Bar, 500 μm . (C) In situ depth profiles of oxygen (square), sulfide (triangle) and pH (circle) collected at peak of photosynthesis (open symbols) or respiration (filled symbols). (D) Cross section of button mat depicting the three spatial regions including an oxic Zone 1 (0 – 3 mm), transitional Zone 2 (3 – 5 mm), and anoxic Zone 3 (5 – 9 mm). Bar, 3 mm.

171x159mm (300 x 300 DPI)

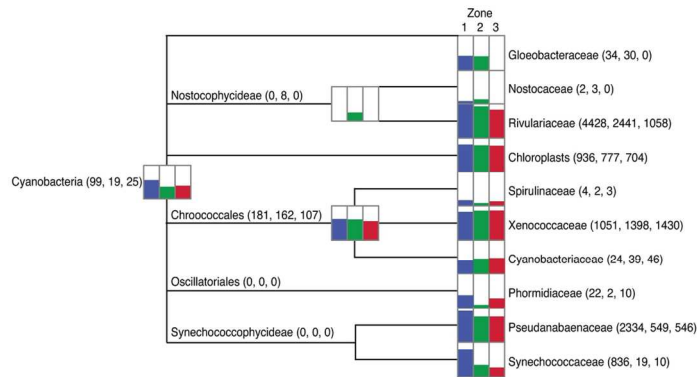


FIG. 2. Taxonomic distribution of cyanobacteria within the thrombolite-forming mats derived from MEGAN5 using the Greengenes database. Read counts are presented logarithmically depicting the distributions for Zone 1 (blue), Zone 2 (green), and Zone 3 (red). Read abundance data for each taxonomic level are included in parentheses.

128x56mm (300 x 300 DPI)

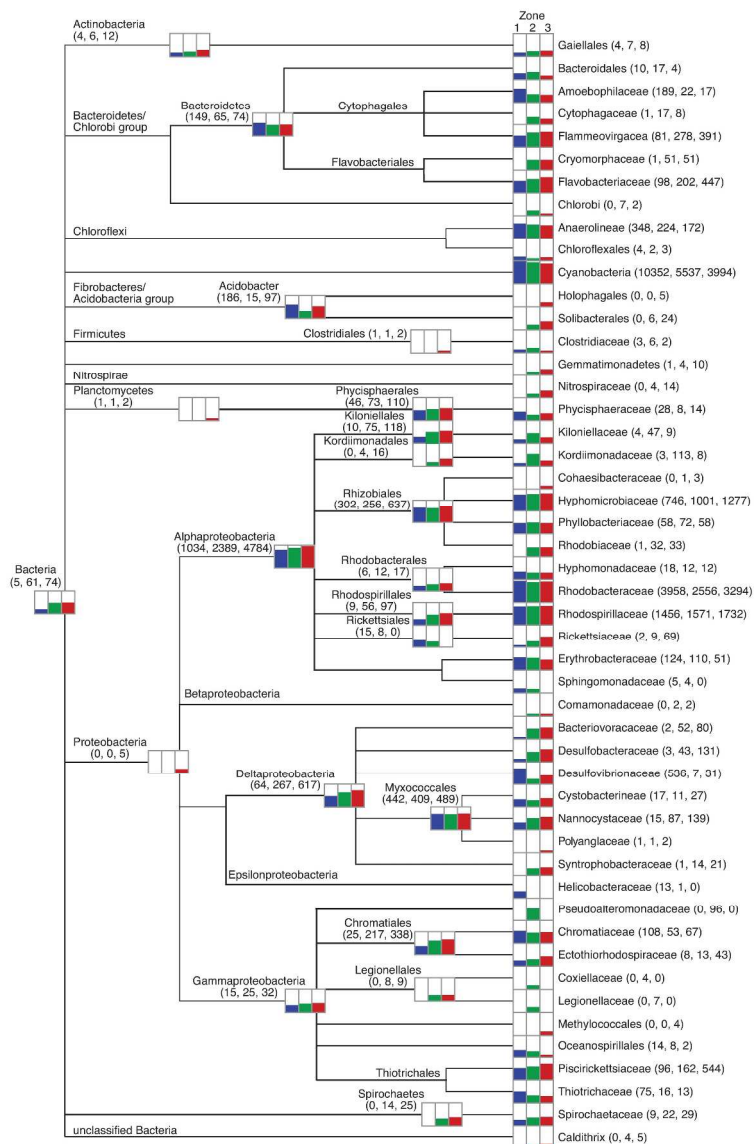


FIG. 3. Taxonomic distribution of Bacteria within the thrombolite-forming mats derived from MEGAN5 using the Greengenes database. Read counts are presented logarithmically depicting the distributions for Zone 1 (blue), Zone 2 (green), and Zone 3 (red). Read abundance data for each taxonomic level are included in parentheses.

246x368mm (300 x 300 DPI)

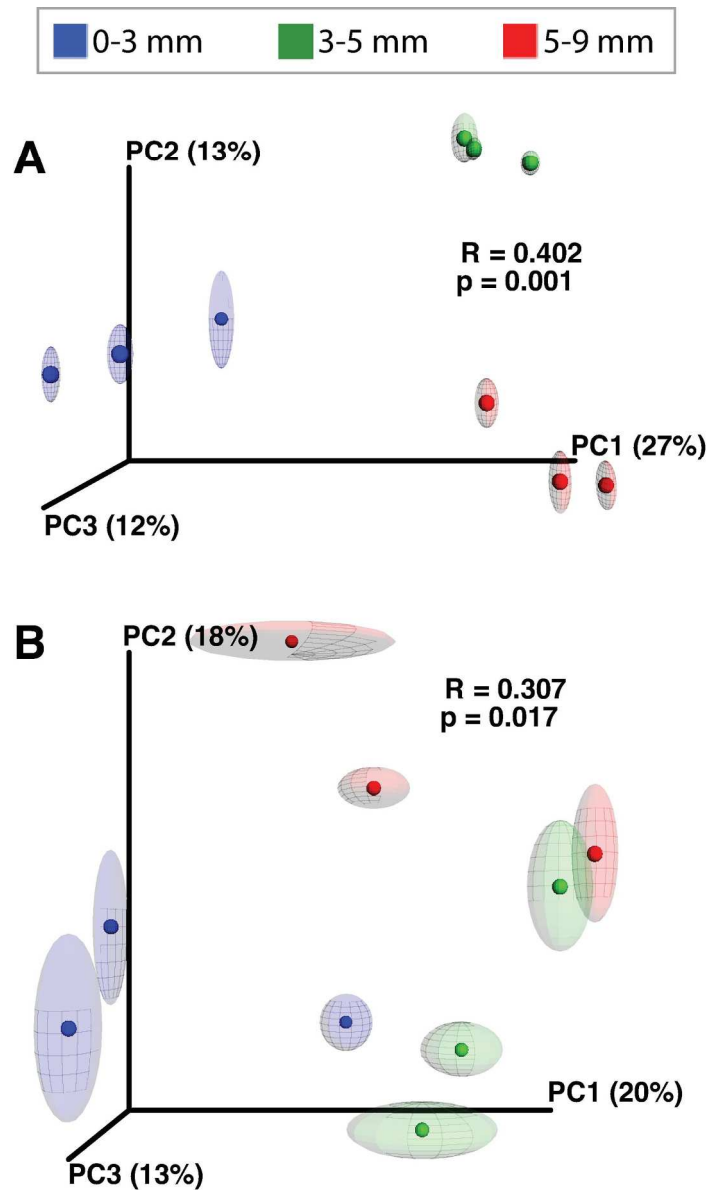


FIG. 4. Comparison of diversity analyses of three spatial zone within the thrombolite-forming mats. Principal coordinate analysis of communities from unweighted UniFrac distance matrix of Zone 1 (0 – 3 mm, blue), Zone 2 (3 – 5 mm, green), and Zone 3 (5 – 9 mm, red) in (A) Bacteria and (B) Archaea populations. Ellipses represent standard deviation over ten rarefaction samplings. Adonis tests suggest that depth is a significant predictor of community composition for both bacterial ($R=0.402$, $p=0.001$) and archaeal ($R=0.307$, $p=0.017$) communities.

146x253mm (300 x 300 DPI)

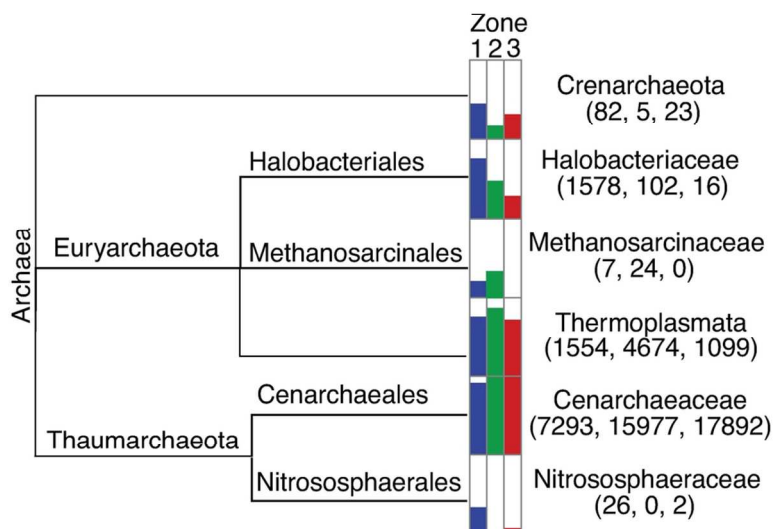


FIG. 5. Taxonomic distribution of Archaea within the thrombolite-forming mats derived from MEGAN5 using the Greengenes database. Read counts are presented logarithmically depicting the distributions for Zone 1 (blue), Zone 2 (green), and Zone 3 (red). Read abundance data for each taxonomic level are included in parentheses.

105x79mm (300 x 300 DPI)

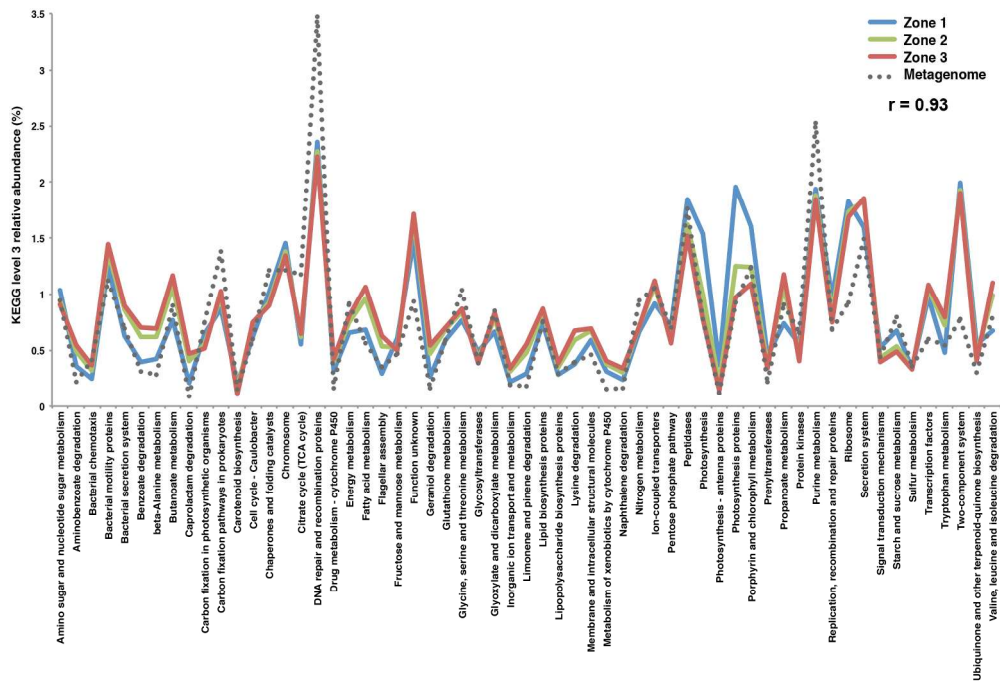


FIG. 6. Functional gene comparison of the three thrombolytic mat spatial zones from 16S rRNA metabolic prediction (PICRUSt) and whole shotgun sequencing. Pearson correlation value (r) is shown for the comparison of metabolic predictions for Zone 1 (blue), Zone 2 (green) and Zone 3 (red) and the whole mat shotgun metagenome.

207x141mm (300 x 300 DPI)

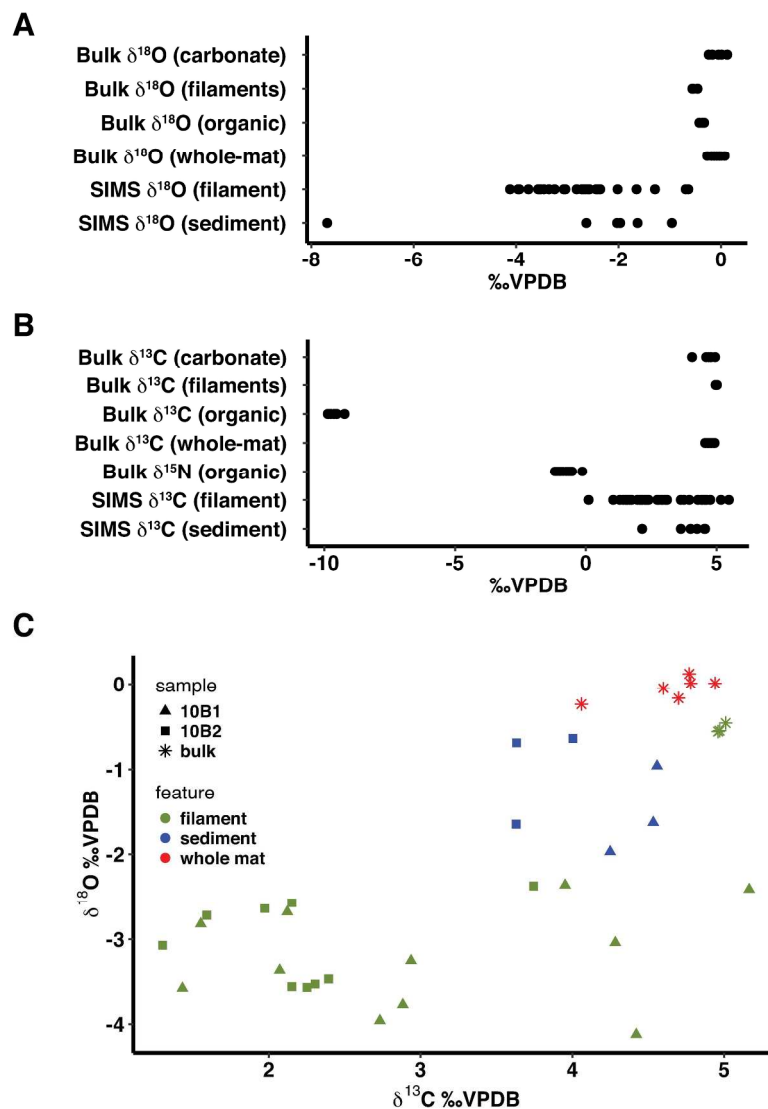


FIG 7. Stable isotope results for calcified filaments located in the upper 3 mm of thrombolite forming button mat. (A) Oxygen isotope values of organic and inorganic fractions using both bulk and SIMS analysis. Analyses were completed for both background carbonate precipitates (sediment), calcified filaments (filaments) and untreated whole mat samples. (B) Carbon and nitrogen isotope values of both organic and inorganic fractions using both bulk and secondary ion mass spectroscopy (SIMS) analysis. (C) Comparative plot of SIMS values collected for oxygen and carbon isotopes. All results are expressed in delta notation with respect to the carbon/oxygen Vienna Peedee Belemnite (VPDB) or nitrogen air (AIR) standard.

239x281mm (300 x 300 DPI)

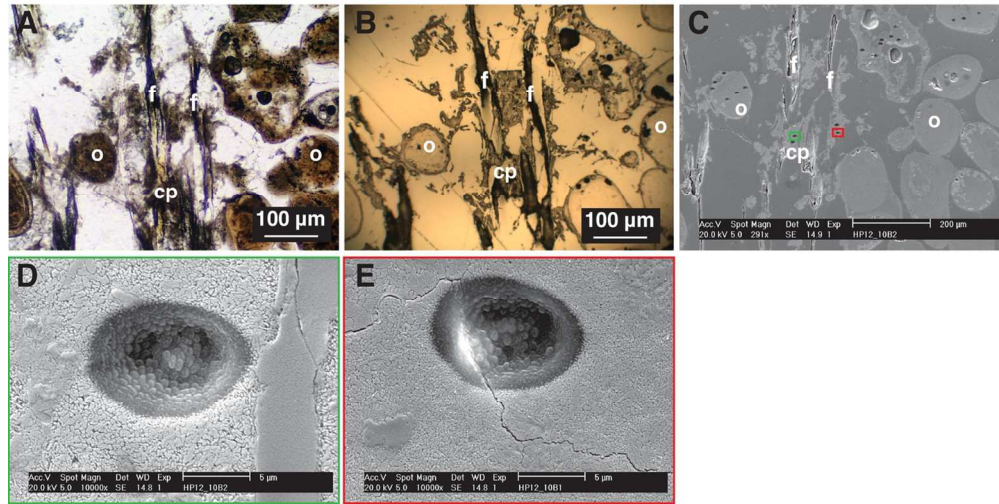


FIG. 8. Overview of target areas for SIMS analyses within the thrombolite forming mat. (A) Petrographic thin section of *Dichothrix* sp. filaments (f) and associated carbonate precipitate (cp) surrounded by sediments such as ooids (o). (B) Gold-coated reflected light image as viewed by the SIMS instrument. (C) SEM micrograph showing the numerous 6-10 μm pits formed during the SIMS analysis. Boxes depict representative pits that show both high (green) and low (red) quality targets within the sample. (D) Higher resolution SEM micrograph of representative high quality pit (corresponding to green box in C) showing no textural anomalies or cracks. (E) SEM micrograph of low quality pit (corresponding to red box in C) showing crack within the targeted sample site. All low quality target sites were removed from down-stream analyses.

123x76mm (300 x 300 DPI)

TABLE 1. SUMMARY STATISTICS FOR THROMBOLITE SAMPLES BY ZONE FOR BACTERIA AND ARCHAEA SAMPLES

	<i>Bacteria</i>			<i>Archaea</i>		
	<i>Zone 1</i>	<i>Zone 2</i>	<i>Zone 3</i>	<i>Zone 1</i>	<i>Zone 2</i>	<i>Zone 3</i>
Depth	0-3 mm	3-5 mm	5-9 mm	0-3 mm	3-5 mm	5-9 mm
No. of Reads	25609	21535	31217	14253	22794	21646
Normalized Reads ^a	3691	3691	3691	3587	3587	3587
Total OTUs ^b	2044	2947	3525	671	506	654
OTUs >0.005%	729	949	956	178	169	172
Shannon Index ^c	6.59	8.67	8.59	4.91	3.58	3.97
±sd	±0.026	±0.026	±0.016	±0.008	±0.020	±0.024
(confidence)	(0.029)	(0.029)	(0.019)	(0.009)	(0.023)	(0.027)
% coverage ^d	94.5	87.8	92.3	97.9	98.2	98.2
±sd	0.13	5.02	0.71	0.07	0.09	0.31

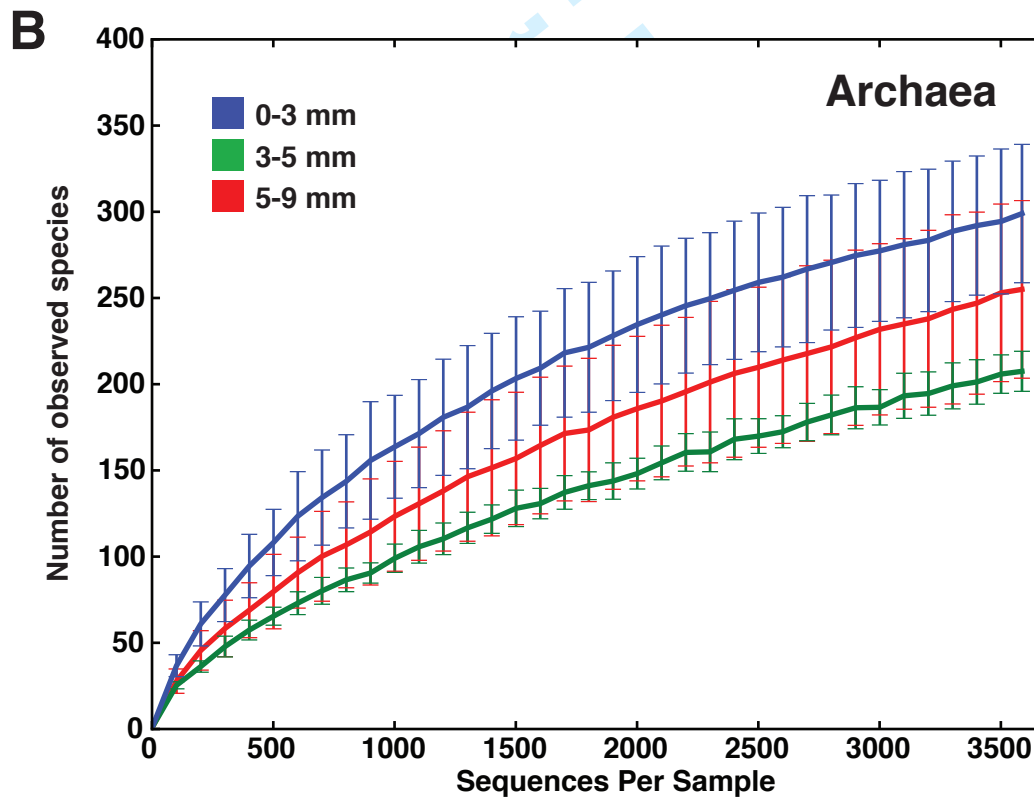
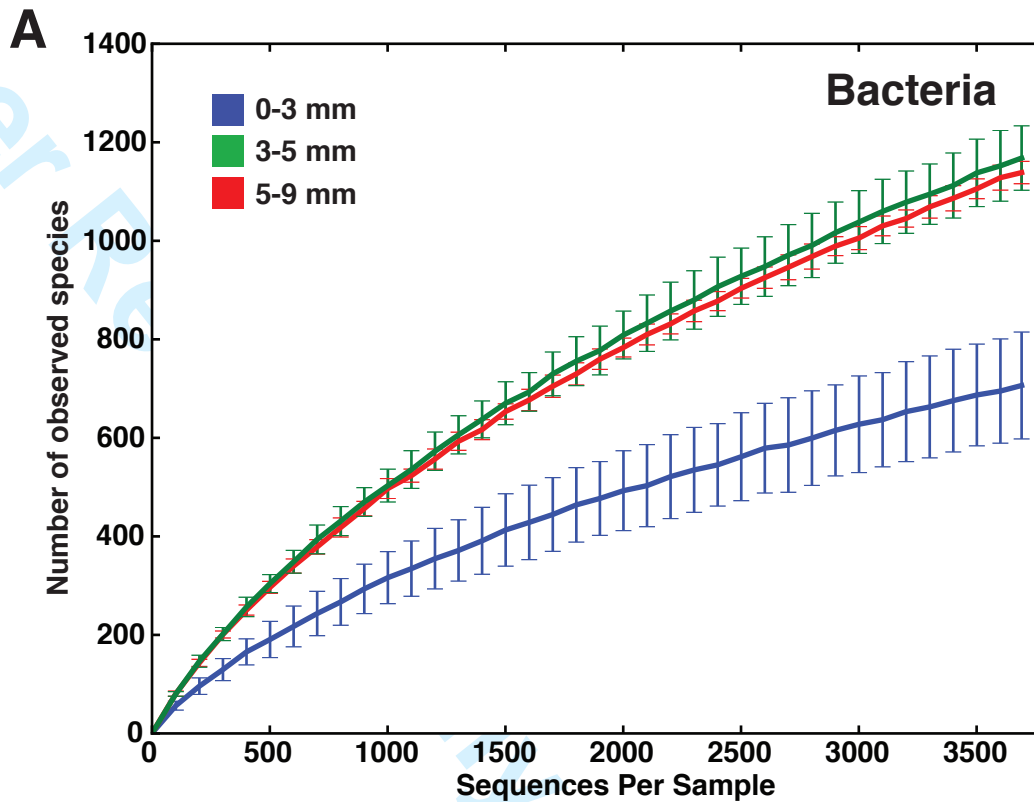
^aRandomized sequence count of each replicate for each zone used to measure diversity.

^bOTU identification used a 97% similarity threshold.

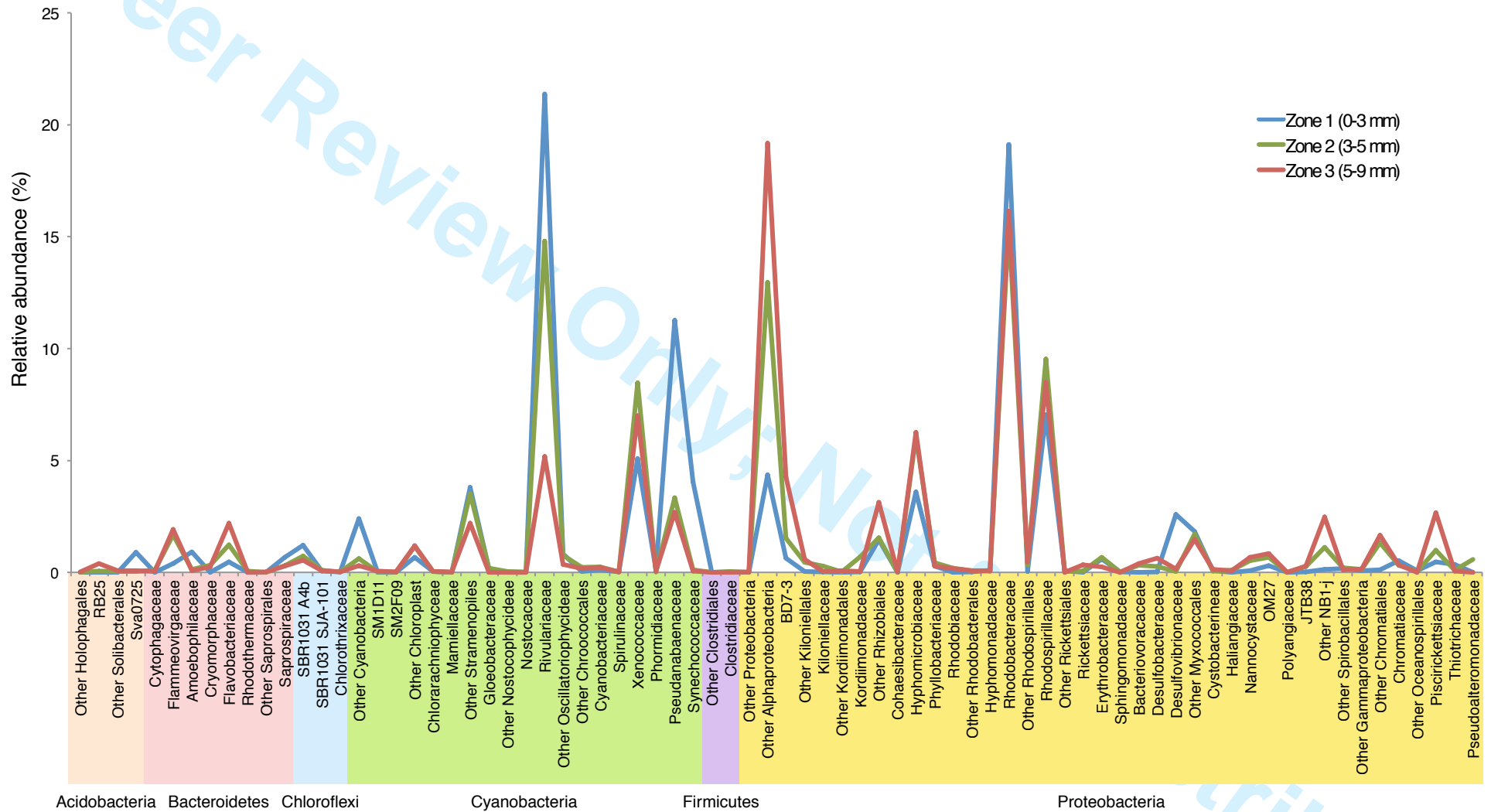
^cShannon diversity index calculated over ten iterations for three replicate samples.

^dGoods coverage estimate.

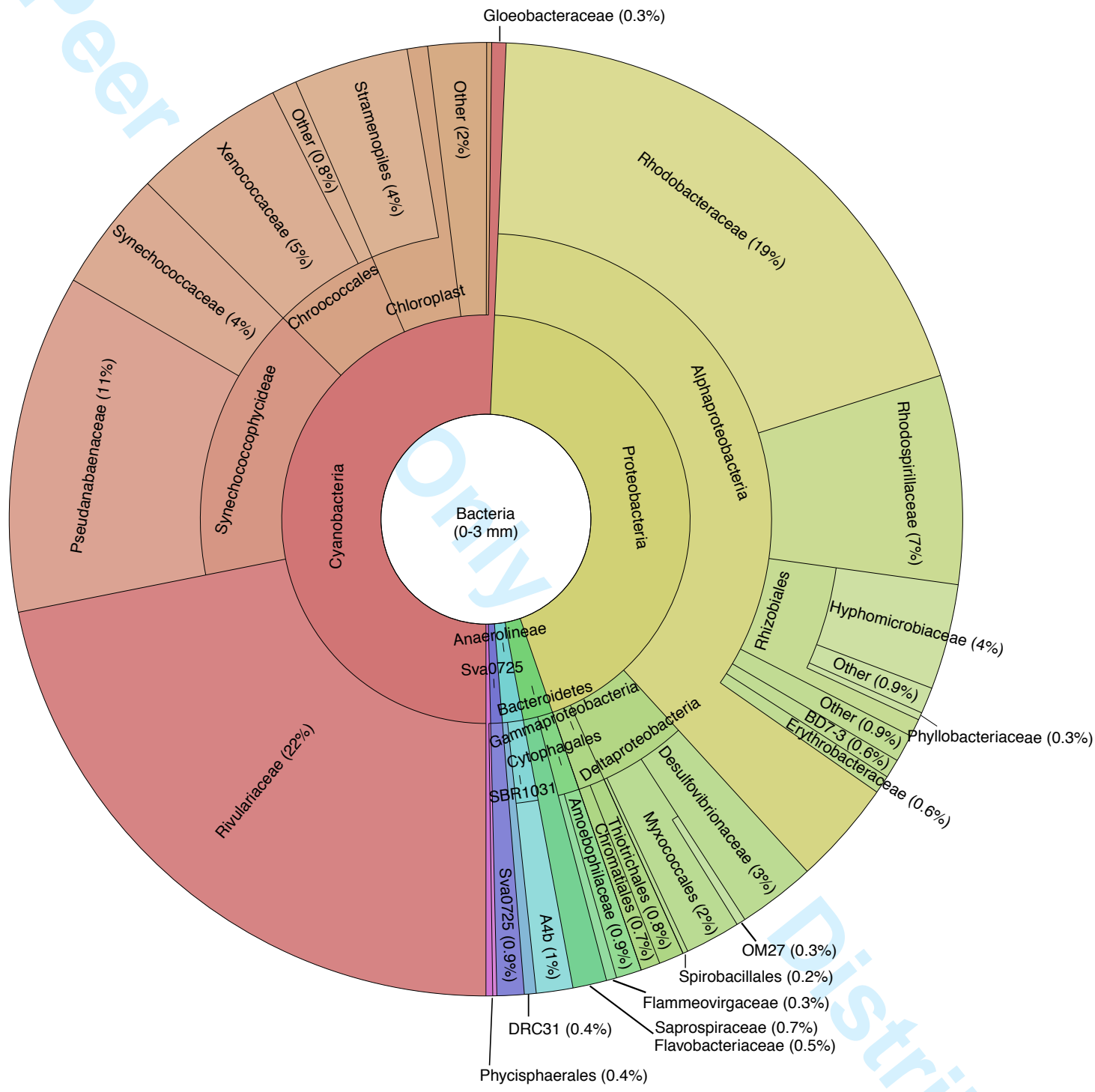
Supplemental Figure S1



Supplemental Figure S2



Supplemental Figure S3



Supplemental Figure S4



Supplemental Figure S5



SUPPLEMENTARY TABLE S1. PRIMER LIST USED TO GENERATE TITANIUM 454 BARCODED LIBRARIES FOR BACTERIA AND ARCHAEA

Specificity	Primer ID	Sample	454 Primer ^a	Barcode ^b	Linker	16S Primer	16S rRNA primer reference ^c
bacteria	Bac27F-T	Bacteria	A	none	TC	AGAGTTTGATCCTGGCTCAG	Suzuki & Giovannoni, 1996
universal	Bac338R-01-T	Zone 1	B	CCAACCTT	CA	TGCTGCCTCCCGTAGGAGT	Suzuki & Giovannoni, 1996
universal	Bac338R-02-T	Zone 1	B	GGAATTGG	CA	TGCTGCCTCCCGTAGGAGT	Suzuki & Giovannoni, 1996
universal	Bac338R-03-T	Zone 1	B	AACCAACC	CA	TGCTGCCTCCCGTAGGAGT	Suzuki & Giovannoni, 1996
universal	Bac338R-04-T	Zone 2	B	TTAAGGCC	CA	TGCTGCCTCCCGTAGGAGT	Suzuki & Giovannoni, 1996
universal	Bac338R-05-T	Zone 2	B	CCGGCCTT	CA	TGCTGCCTCCCGTAGGAGT	Suzuki & Giovannoni, 1996
universal	Bac338R-06-T	Zone 2	B	AAGGCCTT	CA	TGCTGCCTCCCGTAGGAGT	Suzuki & Giovannoni, 1996
universal	Bac338R-07-T	Zone 3	B	AACGAAGC	CA	TGCTGCCTCCCGTAGGAGT	Suzuki & Giovannoni, 1996
universal	Bac338R-08-T	Zone 3	B	TTCGAAGC	CA	TGCTGCCTCCCGTAGGAGT	Suzuki & Giovannoni, 1996
universal	Bac338R-09-T	Zone 3	B	AATACCGC	CA	TGCTGCCTCCCGTAGGAGT	Suzuki & Giovannoni, 1996
archaea	Arc23F ^e	Archaea	none	none	none	ATCCGGTTGATCCTGC	Barns et al., 1994
archaea	Arc958R ^{d,e}	Archaea	none	none	none	YCCGGCGTTGAMTCCATTT	Delong, 1992
archaea	Arc344F-T ^d	Archaea	A	none	TC	ACGGGGYGCGAGCAGGCGCGA	Casamayor et al., 2002
archaea	Arc915R-01-T	Zone 1	B	CCAACCAA	CA	GTGCTCCCCCGCCAATTCCT	Casamayor et al., 2002
archaea	Arc915R-02-T	Zone 1	B	CGAACCAT	CA	GTGCTCCCCCGCCAATTCCT	Casamayor et al., 2002
archaea	Arc915R-03-T	Zone 1	B	AGACAGTG	CA	GTGCTCCCCCGCCAATTCCT	Casamayor et al., 2002
archaea	Arc915R-04-T	Zone 2	B	AGACACAG	CA	GTGCTCCCCCGCCAATTCCT	Casamayor et al., 2002
archaea	Arc915R-05-T	Zone 2	B	CCAACGTA	CA	GTGCTCCCCCGCCAATTCCT	Casamayor et al., 2002
archaea	Arc915R-06-T	Zone 2	B	CATCTCGT	CA	GTGCTCCCCCGCCAATTCCT	Casamayor et al., 2002
archaea	Arc915R-07-T	Zone 3	B	CATCTCCA	CA	GTGCTCCCCCGCCAATTCCT	Casamayor et al., 2002
archaea	Arc915R-08-T	Zone 3	B	CAGTGTGT	CA	GTGCTCCCCCGCCAATTCCT	Casamayor et al., 2002
archaea	Arc915R-09-T	Zone 3	B	CCGATTA	CA	GTGCTCCCCCGCCAATTCCT	Casamayor et al., 2002

- 454 Life Sciences sequence primers A (CTATGCGCTTGCCAGCCCGCTCAG) and B (CGTATCGCCTCCCTCGCGCCATCAG) with a TC or CA linker, respectively, preceding the 16S primer sequence.
- Barcodes sequences from Hamady *et al.*, 2008.
- References are for 16S rRNA gene primer.
- Primers contain degenerate bases: Y (C,T), M (A,C).
- Archaea* specific 16S rRNA gene primers used for initial amplification of a nested PCR.

SUPPLEMENTAL TABLE S3. PERCENT OF KEY ELEMENTS BY WEIGHT
FOUND IN THE THROMBOLITE-FORMING MICROBIAL MAT

	<i>n</i>	%C (s.e.)	%N (s.e.)	%CaCO ₃ (s.e.)
Whole mat	12	12.05 (0.037)	0.17 (0.003)	91.72 (0.24)
Organic	6	43.1 (0.598)	3.26 (0.168)	-
Inorganic	6	-	-	93.33 (0.649)
Filament	1	-	-	45.87 (n/a)